

FORECASTING THE ONSET OF CLOUD-GROUND
LIGHTNING USING S-POL AND NLDN DATA

by

KARTIK RAMAKRISHNAN
B.E. University of Mumbai, 2000

A thesis submitted in partial fulfillment of the requirements
for the degree of Master of Science
in the Department of Department of Electrical and Computer Engineering
in the College of Engineering and Computer Science
at the University of Central Florida
Orlando, Florida

Summer Term
2004

ABSTRACT

The maximum number of thunderstorms in the United States occur in Central Florida. The cloud-ground lightning from these storms is responsible for extensive damage to life and property. The lightning from these storms is also responsible for delays and cancellations of space shuttle launch attempts at the Kennedy Space Center (KSC) and the 45th Space Wing unmanned launches at Cape Canaveral launch facilities. For these and other reasons accurate forecasting of cloud-ground lightning is of crucial importance.

The second phase of NASA's Tropical Rainfall Measuring Mission *Texas and Florida Underflights* project (TEFLUN-B) was conducted between 1st August and 30th September, 1998. The S-band dual-polarization radar (S-Pol) belonging to the National Center for Atmospheric Research (NCAR) was part of the surface based facilities during this project, and was located at Melbourne, Florida. This provided an excellent opportunity to observe Florida thunderstorms with the help of a dual-polarization radar.

This project aims at developing cloud-ground lightning forecasting signatures by analyzing S-Pol data for 10 thunderstorms that occurred over the Kennedy Space Center. Time-height trends of reflectivity, ice and graupel-hail as well as electric potential trends for these storms are taken into consideration while developing the forecasting signatures.

This thesis proposes that a 35dBZ echo at the -5°C temperature level is the best indicator of imminent CG lightning with a POD of 90%, an FAR of 10% and a CSI of 81.8%. An

electric potential level of approximately 1000 V/m also indicates the onset of cloud-ground lightning. An analysis of the microphysical structure of the thunderstorms reveals that the presence of graupel-hail at the -10°C temperature level is necessary in order for cloud-ground lightning to occur.

ACKNOWLEDGEMENTS

I would like to thank my advisor, Dr. Takis Kasparis for giving me the opportunity to work with him on such an interesting project, and for always being there to guide me every step of the way.

I would also like to extend my sincere thanks to Dr. Linwood Jones, for being on my defense committee, and under whose tutelage I have learnt much about radar systems and about the communications field in general.

I would never have been able to manage this project without the help of the people at NCAR and UCAR - Mr. Bob Rilling who painstakingly guided me through the steps necessary to install and use the SOLO software, Mr. Richard Oye who helped out with the hydrometeor classification algorithm for the S-Pol and Dr. Charles Knight who helped me understand the technique of plotting time-height reflectivity contours.

Sincere thanks to Dr. Valliappa Lakshmanan of NSSL for providing me with the WDSS-II software and for helping me install it. Thanks are also due to Mr. Philip Gemmer of the KSC for taking the time and effort to upload the electric field mill data for me at such short notice.

Finally, thanks to Dr. Michael Georgiopoulos for agreeing to be on my defense committee.

TABLE OF CONTENTS

LIST OF FIGURES	vi
LIST OF TABLES	xix
CHAPTER ONE: INTRODUCTION	1
CHAPTER TWO: BACKGROUND	3
2.1: Thunderstorm electrification	3
2.2: Cloud–Ground lightning	9
2.3: Lightning detection at the Kennedy Space Center	13
2.4: Single Polarization Doppler Radars	14
2.5: Dual Polarization Radars	16
CHAPTER THREE: DATA AND SOFTWARE	20
3.1: Lightning data	20
3.2: Radar data	22
3.3: Electric Field Mill data	26
3.4: Sounding Data	28
3.5: Software	28
CHAPTER FOUR: METHODOLOGY	30
4.1: Finding storms using NEXRAD data	36
4.2: Locating a storm using S-POL data	37
4.3: Plotting the time-height trends of ice, graupel and reflectivity	38
4.4: Electric potential trends of the thunderstorms	43

CHAPTER FIVE: CONCLUSIONS	49
5.1: Forecasting Signatures from Reflectivity	50
5.2: Forecasting Signatures from Electric Potential	57
5.3: Forecasting Signatures from graupel-Hail and Ice Trends	57
5.4: Future work	58
APPENDIX: DETAILED STORM ANALYSIS	59
A.1: 19 September 1998 (Cell 92) – storm #1	60
A.2: 26 September 1998 (Cell 75) – storm #2	70
LIST OF REFERENCES	80

LIST OF FIGURES

Figure 2.1: Tripole structure of a thunderstorm cloud	3
Figure 2.2: Thunderstorm electrification due to convection	5
Figure 2.3: Thunderstorm electrification due to induction	6
Figure 2.4: Non inductive theory of thunderstorm electrification	8
Figure 2.5: Effect of an increasing electric field on a water droplet	10
Figure 2.6: CG Lightning discharge processes	12
Figure 3.1: NLDN Sensor Network	20
Figure 3.2: PPI Scan Strategy for the S-Pol	24
Figure 3.3: RHI Scan Strategy for the S-Pol	25
Figure 3.4: Electric Field Mill Network at the KSC	27
Figure 4.1: Location of CG Lightning producing storms	31
Figure 4.2: Location of non- CG Lightning storms	32
Figure 4.3: Output of the SCIT algorithm for Nexrad data	34
Figure 4.4: Lightning producing storm as obtained from Nexrad data	35
Figure 4.5: A set of storms as seen by the Nexrad	36
Figure 4.6: The set of storms in figure 4.1 as seen by the S-Pol	37
Figure 4.7: Time –Height reflectivity contour for a thunderstorm	38
Figure 4.8: Graupel-hail-ice distribution within a thunderstorm	40
Figure 4.9: Sounding data obtained from balloon launches at the CCAFS	42
Figure 4.10: Conversion of co-ordinates from spherical to Cartesian space	44
Figure 4.11: Determining the distance between the storm and field mil	46

Figure 4.12: Electric potential trend of a thunderstorm	48
Figure A.1: Storm#1 as seen by the Nexrad	61
Figure A.2: Time vs. Height reflectivity trend for storm #1	62
Figure A.3: Time vs. Electric Potential trend for storm #1	63
Figure A.4 (a): 0° C level at 18:55:39	64
Figure A.4 (a): 0° C level at 19:01:36	64
Figure A.4 (c): 0° C level at 19:07:04	64
Figure A.4 (d): 0° C level at 19:12:32	64
Figure A.4 (e): 0° C level at 19:18:00	65
Figure A.4 (g): 0° C level at 19:28:49	65
Figure A.4 (f): 0° C level at 19:23:28	65
Figure A.4 (h): 0° C level at 19:34:17	65
Figure A.5: Ice-graupeI-hail trends at the 0° C level for storm #1	65
Figure A.5 (a): -5° C level at 18:55:46	66
Figure A.5 (b): -5° C level at 19:01:43	66
Figure A.5 (c): -5° C level at 19:07:11	66
Figure A.5 (d): -5° C level at 19:12:11	66
Figure A.5 (e): -5° C level at 19:23:35	67
Figure A.5 (f): -5° C level at 19:28:56	67
Figure A.5 (g): -5° C level at 19:34:17	67
Figure A.5: Ice-graupeI-hail trends at the -5° C level for storm #1	67
Figure A.6 (a): -10° C level at 18:55:53	68
Figure A.6 (b): -10° C level at 19:01:51	68

Figure A.6 (c): -10° C level at 19:18:14	68
Figure A.5 (d): -10° C level at 19:23:43	68
Figure A.6 (e): -10° C level at 19:29:03	69
Figure A.6 (f): -10° C level at 19:34:24	69
Figure A.6: Ice-graupe-hail trends at the -10° C level for storm #1	69
Figure A.7: Storm #2 as seen by the Nexrad	71
Figure A.8: Time vs. Height reflectivity trend for storm #2	72
Figure A.9: Time vs. Electric Potential trend for storm #2	73
Figure A.10 (a): 0° C level at 16:25:58	74
Figure A.10 (b): 0° C level at 16:31:10	74
Figure A.10 (c): 0° C level at 16:36:22	74
Figure A.10 (d): 0° C level at 16:41:35	74
Figure A.10 (e): 0° C level at 16:46:47	75
Figure A.10 (f): 0° C level at 16:51:49	75
Figure A.10: Ice-graupe-hail trends at the 0° C level for storm #2	75
Figure A.11 (a): -5° C level at 16:26:04	76
Figure A.11 (b): -5° C level at 16:31:16	76
Figure A.11 (c): -5° C level at 16:36:29	76
Figure A.11 (d): -5° C level at 16:41:41	76
Figure A.11 (e): -5° C level at 16:46:53	77
Figure A.11 (f): -5° C level at 16:52:06	77
Figure A.11: Ice-graupe-hail trends at the -5° C level for storm #2	77
Figure A.12 (a): -10° C level at 16:26:10	78

Figure A.12 (b): -10° C level at 16:31:23	78
Figure A.12 (c): -10° C level at 16:36:35	78
Figure A.12 (d): -10° C level at 16:41:41	78
Figure A.12 (e): -10° C level at 16:46:53	79
Figure A.12: Ice-graupel-hail trends at the -10° C level for storm #2	79

LIST OF TABLES

Table 5.1: Forecasting Matrix for the 35 dBz echo existing at the 0°C level	53
Table 5.2: Forecasting Matrix for the 35 dBz echo existing at the -5°C level	53
Table 5.3: Forecasting Matrix for the 35 dBz echo existing at the -10°C level	54
Table 5.4: Forecasting Matrix for the 40 dBz echo existing at the 0°C level	55
Table 5.5: Forecasting Matrix for the 40 dBz echo existing at the -5°C level	55
Table 5.6: Forecasting Matrix for the 40 dBz echo existing at the -10°C level	56
Table 5.7: Forecasting Matrix for the 45 dBz echo existing at the 0°C level	57
Table 5.8: Forecasting Matrix for the 45 dBz echo existing at the -5°C level	57
Table 5.9: Forecasting Matrix for the 45 dBz echo existing at the -10°C level	58
Table 5.10: POD, FAR and the CSI for each reflectivity lightning signature	59

CHAPTER ONE: INTRODUCTION

The weather in Central Florida is highly conducive to the occurrence of thunderstorms as the Florida peninsula is surrounded by water on three sides. To the west is situated the Gulf of Mexico, while to the east is situated the Atlantic Ocean. Florida also has irregular geographical features like the coastline juts at Apalachicola and Cape Canaveral. Differential heating due to this land-water contrast provides for an abundance of mesoscale thermal boundaries, which serve as lifting/focusing mechanisms for deep convection (Hodanish et al. 1997).

It has been observed that the location of Florida thunderstorms is controlled by the interaction of prevailing low altitude wind and sea breeze circulation (Frank et al. 1967). The maximum numbers of thunderstorms occur in the region just west of the Kennedy Space Center (KSC), where the East Coast Sea Breeze (ECSB) forms along the coast during the morning and moves inland during the afternoon. Also there is a West Coast Sea Breeze (WCSB) that is caused by the temperature difference between the Gulf of Mexico and the Florida peninsula. When the ECSB and WCSB collide they trigger numerous thunderstorms over the Florida peninsula.

Interactions between the various fronts off the Atlantic Ocean, Gulf of Mexico and the other numerous bays, rivers and outlets are thus responsible for the occurrence of thunderstorms

(Roeder et al. 2000). Cloud-ground lightning from these thunderstorms is at a maximum during the summer months of June through September. The number of strikes varies from approximately 10 strikes per square kilometer along the coast to 30 strikes in an area about 8 miles to the west of the Shuttle Landing Facility at the KSC (Hodanish et al. 1997). Cloud-ground lightning from Florida thunderstorms around the KSC and Cape Canaveral, accounts for 90% of the annual total. The lightning from these storms has a profound impact on life and property. A study has revealed that Florida had the largest number of injuries and deaths caused by lightning during the period 1959-2001. Cloud-ground lightning also affects launch operations at the KSC and Cape Canaveral Air Force Station (CCAFS). Ground processing operations required for launches must cease during thunderstorms to protect personnel and expensive equipment. This causes costly delays in launch preparation. Approximately 1/3 of space launch countdowns are delayed or scrubbed due to lightning (Hazen et al. 1995). The forecasting of cloud-ground lightning from thunderstorms is hence of paramount importance.

Several signatures to forecast cloud-ground lightning have already been developed in the past. These signatures rely primarily on analyses of radar data. The next chapter provides an insight into the process of thunderstorm electrification and the already existent CG lightning forecasting techniques.

CHAPTER TWO: BACKGROUND

2.1 Thunderstorm electrification

A convective cloud that is capable of producing lightning is by definition a thunderstorm cloud. In order to produce lightning it is necessary for some sort of electric field to exist within the cloud. Studies suggest that particles within a thunderstorm cloud do carry charge, and several theories have been put forth to explain the charging process. These theories are discussed in the following paragraphs.

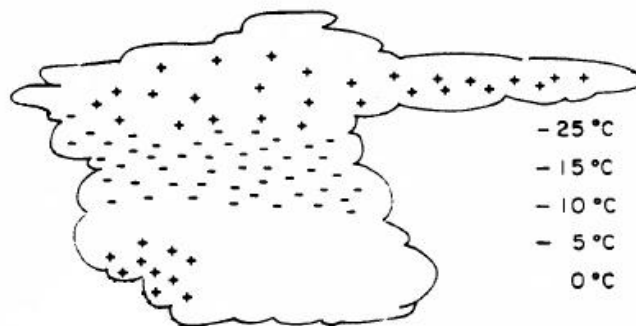


Figure 2.1- Tripole structure of a thunderstorm cloud

Figure 2.1 shows the charge structure within a thunderstorm cloud. As can be seen there are positive charges situated in the upper part of the cloud, while negative charges are situated at a lower altitude. There also a few positive charges situated at the base of the cloud, commonly referred to as *pocket charges*.

In order for any thunderstorm electrification theory to be considered valid, it must satisfy the following requirements necessary for the observed electric field development.

There must be, on an average, 20-30 minutes of lightning and precipitation from the thunderstorm cell.

The average electric moment destroyed in a lightning flash should be approximately 100 Coulomb km, with a corresponding charge of 20-30 Coulombs.

Charge generation and separation should take place between the -5 and -40 degree levels.

The negative charge center should be located near the -10 degree level, while the positive charge center should be located a few kilometers higher up in the cloud.

Sufficient charge separation should occur in order to cause the first lightning discharge within 10-15 minutes of the appearance of radar-detectable precipitation.

The *convection theory of electrification* states that a fair weather field causes the lower troposphere to have a net positive charge. When a thunderstorm cloud begins to form, convective

updrafts cause these positive charges to rise to the upper portion of the cloud, where they encounter air in which the mobility of free ions is directly proportional to the altitude. The free negative ions in the air are attracted by the positive charges present at the top of the cloud, but instead of neutralizing these positive charges, they are brought to lower portions of the cloud by the convective downdrafts. This process continues leading to an exponentially increasing rate of cloud polarity. Figure 2.2 depicts this process.

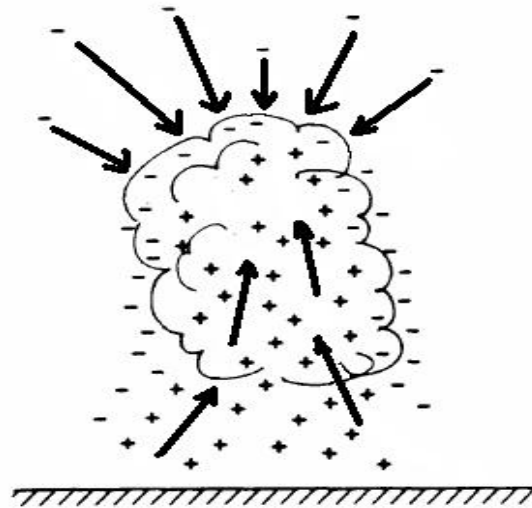


Figure 2.2- Thunderstorm electrification due to convection

The *induction charging theory* states that the presence of the fair-weather field causes cloud

particles to become polarized. The lower part of the particle becomes positively charged while the upper part acquires a negative charge. It is hypothesized that when a small cloud droplet collides and rebounds from a precipitation particle, the larger particle becomes negatively charged, while the smaller particle becomes positively charged. The larger particles then move downwards against the updraft to lower portions of the cloud while the smaller positively charged particles are swept by the updrafts to the upper portion of the cloud, leading to charge separation. Figure 2.3 shows the process of electrification as stated by this theory.

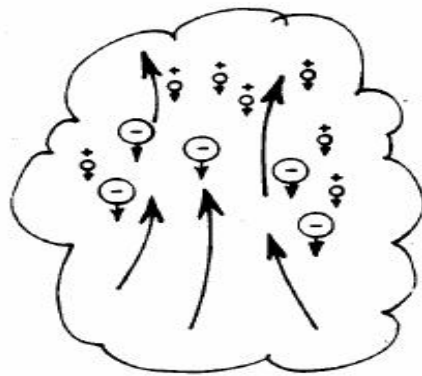


Figure 2.3- Thunderstorm electrification due to induction

The electrification process in a thunderstorm can also occur due to the *non-inductive charging* of graupel and ice particles. Graupel is formed when snow crystals collide with liquid water

droplets in the cloud. The water droplet freezes on contact with the snow crystal and thus a snow crystal with distorted geometry is obtained. When graupel pellets collide with ice crystals they acquire a negative charge while the ice particles acquire a positive charge.

The ice crystals are lifted to the upper portion of the cloud while the negatively charged graupel pellets move to a lower altitude, which is typically the -10 degree isotherm. However in order to account for the tripole structure of a thunderstorm cloud the theory suggests that the polarity acquired by the particles after collision is dependant on temperature.

Above a certain temperature level, the ice crystals charge positively while the graupel charges negatively. Below this temperature level, graupel pellets charge positively and move to the base of the cloud while the ice crystals acquire a negative charge and move upwards to some altitude. The isotherm at this altitude is known as the *reversal temperature*, and it is where the negative charges are located. Figure 2.4 depicts the non-inductive charge theory.

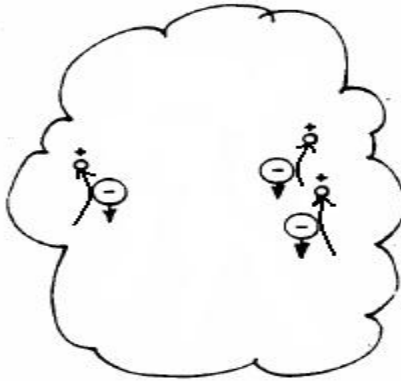


Figure 2.4- Non inductive theory of thunderstorm electrification

While the above theories suggest a means for electrification to occur within a thunderstorm cloud, the actual mechanisms responsible for charge transfer and separation have yet to be universally agreed upon. It is quite simple to explain the charge transfer between two conducting particles, but precipitation particles in a thunderstorm have varying surface conductivities which may limit the transfer of charge. It is also quite possible that collisions between particles may not really be necessary in order for electric fields to occur. The fact that ions can be absorbed by cloud particles and then carried by convection currents to form accumulated charge centers is a distinct possibility.

2.2 Cloud-Ground Lightning

Lightning can be defined as an electrical discharge in the atmosphere. Lightning occurs when there is an electrical breakdown of insulating air and resulting ionization (plasma) thus providing a conductive path along which current can flow.

A water droplet in a thunderstorm cloud located between the negative charge center and the positive charges at the base of the cloud has a positively charged upper surface and a negatively charged lower surface, which is flat due to air pressure. As the electric field between the charge centers increases, the drop becomes elongated in the direction of the charge centers. When the field value reaches approximately 1000 KV/m, there is a glow discharge in the form of filaments from the positive and negative sides of the drop, stretching towards the charge centers. This discharge is termed as a *corona discharge*. The filament towards the negative charge center is usually longer than the filament in the direction of the positive charge center. Eventually the water droplet breaks into minute positively charged ions, which are attracted towards the negative charge center. Thus a conducting path is formed between the negative charge center and the positive charge center at the base of the cloud. Positive charges from the base of the cloud are deposited along the discharge channel. This process is shown in figure 2.5.

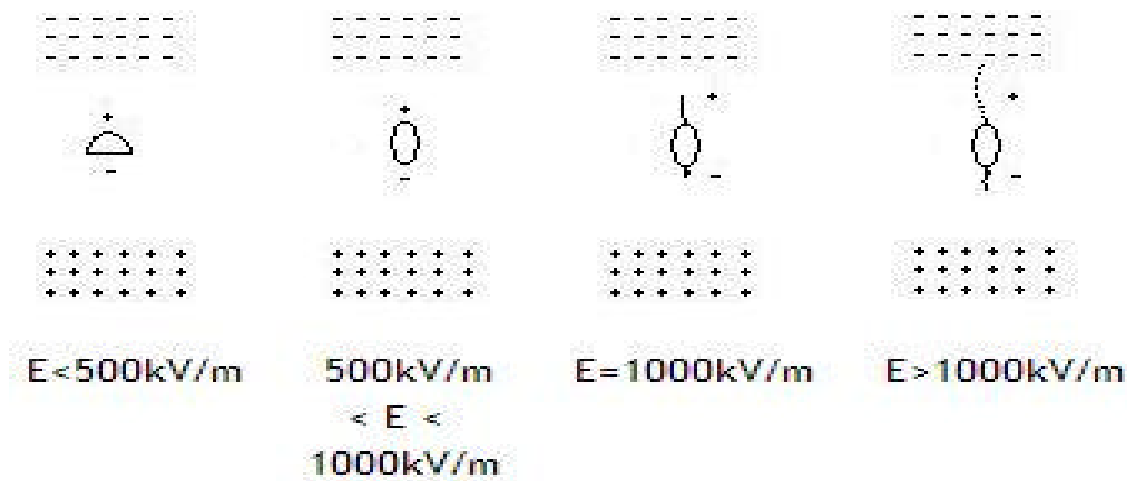
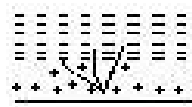


Figure 2.5- Effect of an increasing electric field on a water droplet

After this channel has been established, the electric field between the negative and positive charges continues to increase. When the electric field is high enough, negative charges from the negative charge center flow down to the cloud base, neutralizing the positive charges present along the channel. As a result, a high negative potential is created at the base of the cloud. The electric field continues to increase until it reaches a value of 6000 kV/m. At this point, a negative leader streamer begins to move towards the ground in a stepwise fashion. This streamer is called the *stepped leader*. It moves with an average velocity of $3 \times 10^5 \text{ m/s}$, reaching the ground in

approximately 10 ms, and bringing a high negative potential along the channel to the ground. When the stepped leader is very close to the ground an electrical breakdown occurs between the tip of the leader and the ground causing a positive streamer to shoot from the ground towards the leader tip. When it meets the leader, the potential at the tip is raised to the potential of the ground, while the rest of the channel is at a high negative potential.

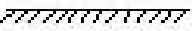
This causes the positive streamer to shoot up the channel to the base of the cloud, depositing positive charges along the way. This positive streamer is termed as a *return stroke*. If fresh negative charge is transferred to the previous return stroke channel from the negative charge center (*J process*), a new leader emanates from the base of the cloud to the ground. This leader is called a *dart leader*. The entire process leading to a ground discharge is shown in Figure 2.6.



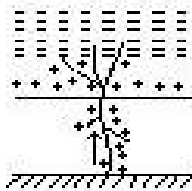
Breakdown within the cloud- positive charges deposited along the discharge channel



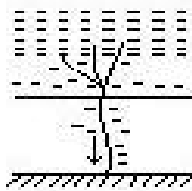
Negative charges from the charge center neutralize the positive pocket charges at the base of the cloud



Electric field value reaches 6000kV/m
Stepped Leader originates from the cloud towards the ground



Return stroke triggers from the ground depositing positive charges along the discharge channel and at the cloud base



Negative charge is transferred from negative charge center to cloud base resulting in a dart leader

Figure 2.6- CG Lightning discharge processes

2.3 Lightning Detection at the Kennedy Space Center

The 45 Weather Squadron (45 WS) provides weather support to America's space program at the CCAS and the KSC on the Central Florida Atlantic coast (Roeder 1998). As mentioned earlier, cloud-ground lightning strikes delay launch activities from the KSC and CCAS. To help reduce these delays, the 45 WS provides two types of lightning watches and lightning warnings for 5 NM radii circles centered on 11 operationally significant sites, six on the CCAS, four on the KSC, and one on the Patrick Air Force Base (Roeder 1998). A lightning watch forecasts conditions for lightning to occur within 30 minutes, while a lightning warning is issued when lightning is imminent or occurring.

Several weather systems to detect and forecast lightning are used by the 45 WS. The Lightning Detection And Ranging (LDAR) consists of 7 antennas and uses the Time Of Arrival (TOA) system to determine the location of various types of lightning (in-cloud, cloud-cloud, cloud-ground etc.). The Cloud to Ground Lightning Surveillance System (CGLSS) with 5 antennas is a magnetic direction finding system. The Launch Pad Lightning Warning System (LPLWS) is a network of 31 surface electric field mills.

The 45 WS also uses the WSR -74C and WSR-88D weather radars to make lightning forecasts. Empirical lightning forecasting techniques used by the 45 WS have been developed over several years and are classified into two categories: nowcasting and longer-than-nowcasting. Nowcasting techniques are used to support the lightning watch and warning duties while longer-than-nowcasting techniques support other operational and planning techniques (Roeder, 1998).

2.4 Single Polarization Doppler Radars

Most cloud-ground lightning signatures based on Doppler radar analyses are stated in terms of the presence of a particular reflectivity echo at a particular temperature level. The echo and temperature levels are chosen at the discretion of the researcher. Already existent signatures in terms of reflectivity echoes are discussed in the following paragraph. Signatures based on factors like wind velocity in a thunderstorm, or the amount of Liquid Vertically Integrated Liquid (LVIL) also exist and are discussed later in the chapter.

Research has shown that electrification in clouds is closely related to the -10°C temperature level (Takahashi, 1984). The radar nowcasting technique for CG lightning used by the 45 WS states that an echo within the 45-48 dBz range must exist at least 3000 feet above the -10°C

isotherm for 10-15 minutes (Roeder, 1998). A study by Steven G. Hoffert (Penn State University) indicated that a 10 dBz echo at or above the freezing level (approximately 4km above ground level) indicates imminent CG lightning. The study also stated a 30 dBz echo at or above the -15°C to -20°C level as a signature. The median lead time between the presence of the first 10 dBz echo at the freezing level and the occurrence of the first cloud-ground lightning flash was observed to be approximately 15 minutes. A study of reflectivity echoes at various temperature heights in Florida thunderstorms revealed that the 40 dBz echo at the -10°C temperature level was the best indicator of cloud-ground lightning with a POD of 84% and an FAR of 7% (Gremillion, 1999). A 25 dBz echo at the -15°C level and a 20 dBz echo at the -20°C level were other signatures observed to be good cloud-ground lightning indicators. A study of radar echoes in the Hokuriku District, Japan revealed that the first lightning discharge occurred after the 30 dBz echo exceeds the -20°C level (Michimoto, 1991). Physically, echoes like the 10 dBz, 20 dBz, 30 dBz etc. indicate the presence of a large amount of mixed-phase precipitation. Updrafts and downdrafts play a crucial role in the charge-separation process, and their contribution cannot be overlooked. Studies have shown that strong updrafts exist in clouds that produce cloud-ground lightning and are responsible for carrying graupel to the top of the cloud, while downdrafts carry ice particles to the lower part of the cloud. Collision between the two particle types leads to charge separation. The charge separation process leads to the formation of

an in-cloud discharge, which then becomes the precursor to the formation of the cloud-ground discharge.

A recent study has also shown that the amount of Liquid Vertically Integrated Liquid (LVIL) is a good forecasting signature to predict the onset of cloud-ground lightning. LVIL refers to the amount of liquid water content present in a thunderstorm cloud. LVIL amounts of 0.5 mm in the -10 to -15 ° C layer simultaneously with amounts of 0.25 mm in the -15 to -20 ° C layer indicate that lightning is imminent, with a POD of 96% and an FAR of 21%.

Having thus gained a brief insight into the various signatures that are used to predict the onset of cloud-ground lightning, we now turn our attention to dual-polarization radars.

2.5 Dual Polarization Radars

This section begins with a brief overview of a dual-polarization radar and a description of the various parameters that can be observed with such a radar, before moving on to precipitation classification using and lightning studies performed using dual-polarization radars.

A single-polarization Doppler radar transmits pulses of a single polarization type, either vertical or horizontal. Here polarization of the pulse refers to the orientation of the electric field in the free-space propagating wave. A dual-polarization radar on the other hand alternately transmits pulses with vertical and horizontal polarization. A single-polarization Doppler radar is able to use the *Doppler shift* phenomenon to determine wind speed or cloud motion. However, being able to transmit pulses of a single polarization type implies that it can observe particle interaction in only one dimension, as opposed to the dual-polarization radar, which can observe particles in two dimensions, including differential propagation effects. Thus the dual-polarization radar is much better at characterizing cloud precipitation

Since a dual-polarization radar can measure both horizontal and vertical polarizations the power returns can be compared in a variety of ways to obtain information about the precipitation particle types in a cloud. Listed immediately, are some of the parameters that can be observed by a dual-polarization radar,

- ? Differential Reflectivity (ZDR): The ratio of the reflected horizontal power return to the vertical power returns. This is a good indicator of drop shape.
- ? Correlation Coefficient (RHO): The correlation coefficient is a correlation between the reflected horizontal and vertical power returns. It is a good indicator of regions where there is a mixture of precipitation types, such as rain and snow.
- ? Linear Depolarization Ratio (LDR): The LDR is the ratio of the vertical power return from a horizontal pulse or the horizontal power return from a vertical pulse. It is a good indicator of the mixed –phase region.
- ? Specific Differential Phase (KDP): The specific differential phase is the returned phase difference between the horizontal and vertical pulses for some specific range measurement. It is a very good estimator of rain rate.

The power reflected back to a radar by the various types of precipitation particles present in the cloud is a complex function of the shape and size of the particle that reflects it. Several algorithms have been developed which use the data from a dual-polarization radar to identify the precipitation particles within the cloud. Typically, combinations of two or more observables are used to identify precipitation types in a cloud. Studies have shown that a dual-polarization radar can be used to distinguish between solid and liquid precipitation in a storm, and also locate ice-crystal populations in storms that are electrified.

Dual-polarization radars, can also be used to study storms that produce cloud-ground lightning. Several lightning producing clouds in Japan were studied using a C-band dual-polarization radar in 1994. The study revealed that before a cloud-ground lightning strike occurred, graupel particles were lifted 3-4 km near the cloud top and then descended to the cloud base, while ice particles rose continuously to the cloud top (Maekawa,1994). This suggested that electrification in the thunderstorm cloud occurred as a result of collisions between ice and graupel.

The Convection and Precipitation/Electrification (CaPE) experiment was conducted in the summer of 1991. The CP-2, a dual-polarization radar developed by NCAR was used to observe Florida thunderstorms at Cape Canaveral and gain an insight into the electrification process of a thunderstorm. Analysis of storms using the radar proved that the onset of electrification coincided with the appearance of significant volumes of differential reflectivity, which indicated the presence of raindrops with diameters larger than 2 mm. There was also the near simultaneous presence of a large amount of depolarization, which was indicative of the freezing of these raindrops (Jameson, 1994).

The Severe Thunderstorm Electrification and Precipitation Study (STEPS) was conducted in Eastern Colorado and Western Kansas during the months of May- July 2000. A dual-polarization

radar was used to observe thunderstorms during this project. Analysis of the radar data indicated that in order for lightning to occur, radar echoes of 40 dBz had to exist at altitudes greater than 7 km MSL. Storms that produced only in-cloud lightning and storms that went on to produce cloud-ground lightning differed in the altitudes at which the lightning strikes originated. Positive and negative cloud-ground strike producing storms could be differentiated by the time between the first 25 dBz echo and the first in-cloud strike.

The next two chapters discuss in detail the data and software used for this project, and the way in which the data was analyzed to obtain the required results.

CHAPTER THREE: DATA AND SOFTWARE

3.1: Lightning data

Lightning data from the National Lightning Detection Network (NLDN) was used for this project. The NLDN is a commercial lightning detection network operated by Global Atmospheric Inc. (GAI). The network consists of over 100 remote, ground-based facilities spread all over the United States. Figure 3.1 shows the location of the various NLDN sensors throughout the United States.



Figure 3.1- NLDN Sensor Network

These facilities are capable of detecting the electromagnetic signals given off by lightning strikes when they hit the ground. These remote sensors then send data via a satellite link to the main control center. The control center processors then analyze the data and determine the location, time, polarity and amplitude of each strike. The remote locations make use of direction finders as well as Time Of Arrival (TOA) methods to determine the exact location of a lightning strike.

3.2: Radar data

Radar data from the S-Pol and the WSR-88D at Melbourne (KMLB) was used for this study. The KMLB WSR-88D is used in support of the NWS and the space-launch community. It has a 0.95° beam-width and employs two scan strategies viz. the VCP11 and the VCP21. VCP stands for *Volume Coverage Pattern*. The VCP11 is a deep convection scan and has an update rate of 5 minutes. The radar moves through a set of fourteen elevation angles between 0.48° and 19.51° . The VCP21 is the standard precipitation scan during which the radar covers a set of nine elevation angles every 6 minutes.

The S-Pol was developed at the National Center for Atmospheric Research (NCAR). It is a dual polarization weather radar which operates in the S-band (2700-2900MHz). It has a beam-width of 0.93° and a peak transmitting power of 1.2 Megawatts. The S-Pol has three types of scan

strategies, the Surveillance scan (SUR), the Plan Position Indicator (PPI) and the Range-Height Indicator (RHI). In the SUR mode the S-Pol scans cycles through a range of azimuths at a fixed elevation angle of 0.5° . The SUR scan may reach the freezing level but at a distance that is very far away from the S-Pol. Hence such a scan is of no practical importance to this study. Thus scan days with only SUR scans were not considered during this study. In the PPI mode, the S-Pol scans through a set of elevation angles. For each of the elevation angles, it also scans a set of sectors in the azimuth. In the RHI scan mode, the S-Pol scans over a set of sectors in the azimuth, and for each of these sectors it scans through a set of elevation angles. The S-Pol scans above the freezing level in both the PPI and RHI modes. All storms considered for this study had data in the form of PPI scans.

Figure 3.2 shows a PPI scan for 18th September 1998. The parameter depicted in the scan is reflectivity (DZ). The S-Pol is located at the center of the scan, and the concentric circles indicate the range at every 10 km. The color bar at the bottom of the scan is an indicator of the reflectivity range in dB. The lines intersecting the concentric range circles at every 30° indicate sectors in the azimuth sectors from 0° to 360° .

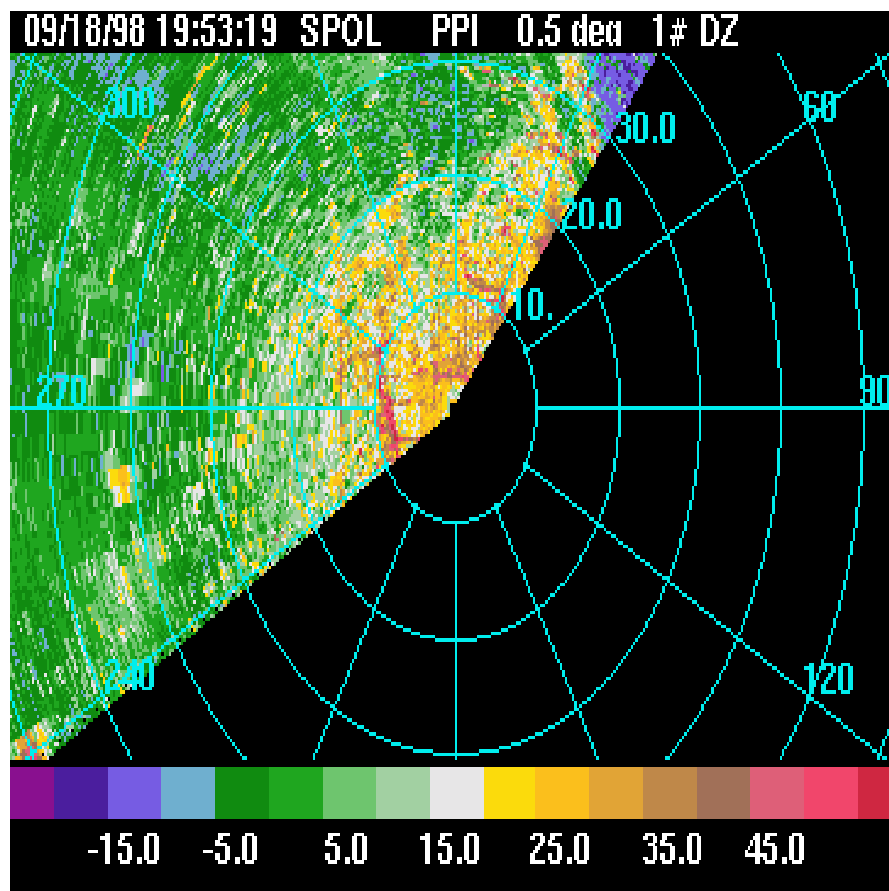


Figure 3.2 – PPI Scan Strategy for the S-Pol

Figure 3.3 shows an RHI scan for 29th July 1998. In this type of scan, the 90° azimuth line actually indicates the 0° elevation angle. Thus, in figure 3.3, the S-Pol has scanned between elevation angles of 0° to 30°. The concentric circles denote the range at every 10km like they do

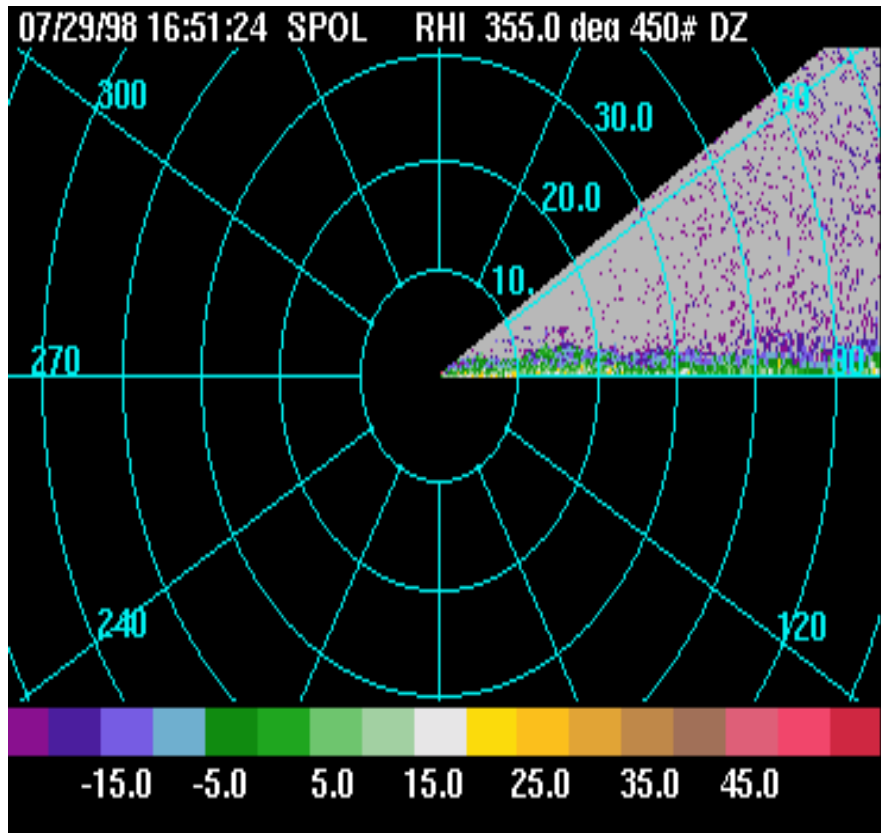


Figure 3.3 – RHI Scan Strategy for the S-Pol

in the PPI scans. The Nexrad radar at Melbourne (KMLB) is located at 28.11N and 80.65W. For the TEFLUN-B project, the S-Pol was located at 27.89N and 80.745W, 26 km south-southwest of the KMLB. Thus, the storms that could be detected by the Nexrad radar could also be detected by the S-Pol..

3.3: Electric Field Mill Data

There are in all 31 field mill sites in the electric field mill network- 23 sites at the KSC and 8 sites at the CCAFS. These mills form part of the Launch Pad Lightning Warning System (LPLWS). These mills are designed to measure the electric field intensity at ground level. They can thus provide data on lightning activity and surface electric fields induced by charge aloft. This data helps forecasters determine when electric charge aloft may be sufficient to create triggered lightning during launch, and to determine when to issue and cancel lightning advisories and warnings. The electric field mill network at the KSC is shown in figure 3.4.

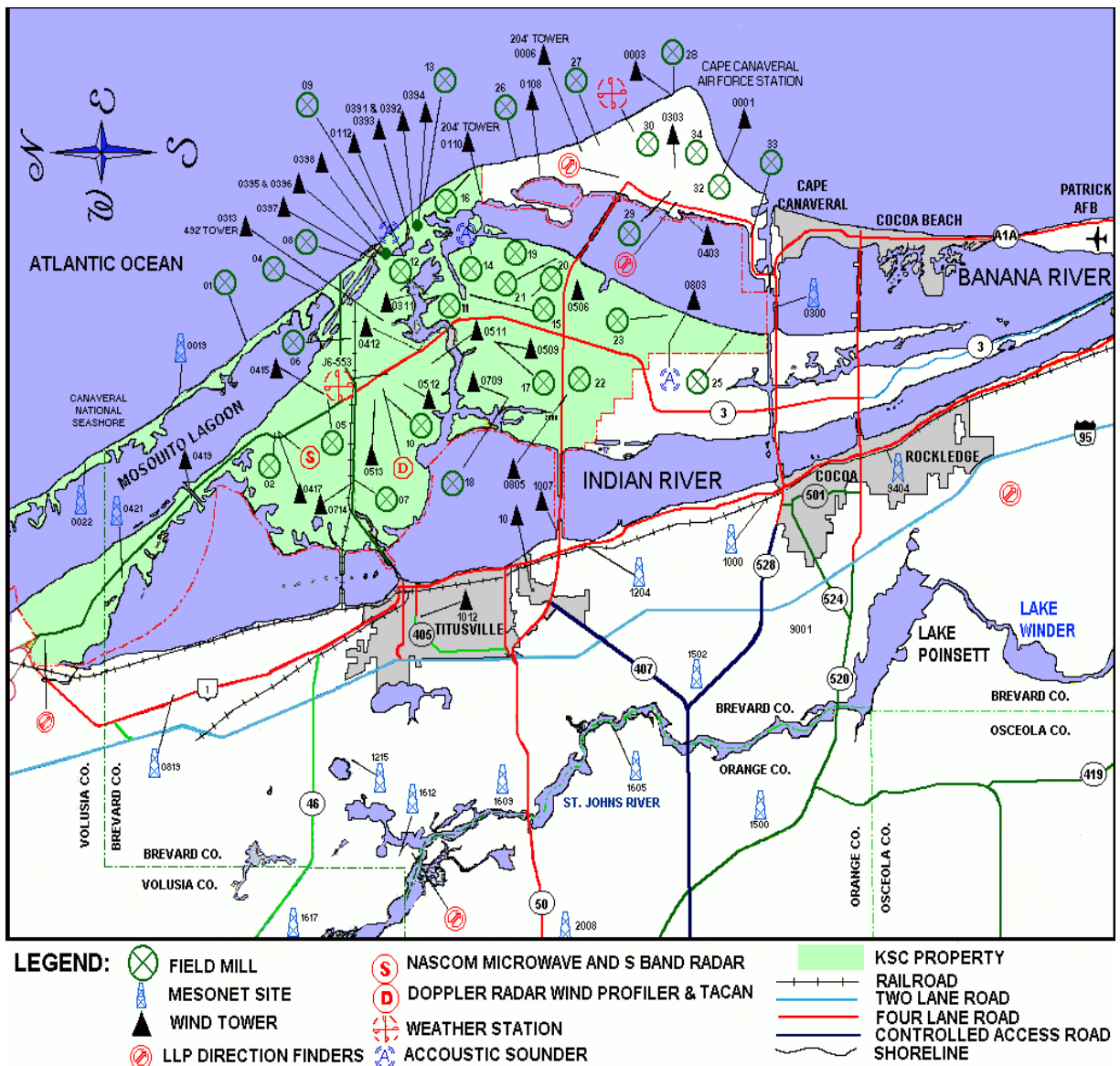


Figure 3.4: Electric Field Mill Network at the KSC

3.4: Sounding Data

Sounding data for the storms was obtained from balloon soundings. These balloons were sent up twice everyday during the summer months of 1998, from the Cape Canaveral Air Force Station.

3.5: Software

The Warning Decision Support System- Information Integrated (WDSS-II) developed by the National Severe Storms Laboratory (NSSL) was used to process and display NEXRAD level II data as well as the NLDN lightning data. The WDSS-II interface allows the user to overlay and manipulate data from various radars and some environmental sensors. The single-radar NSSL algorithms include the Storm Cell Identification and Tracking (SCIT) algorithm, Hail Detection Algorithm (HDA), Tornado Detection Algorithm (TDA), Mesocyclone Detection Algorithm (MDA), and the Damaging Downburst Prediction and Detection Algorithm (DDPDA).

In order to display S-Pol data, SOLO, software developed by the Atmospheric Technology Division (ATD) was used. The software enables the user to display and manipulate data in the DORADE format. SOLO can also be used to view the results of a particle identification

algorithm that identifies and classifies hydrometeors from the S-Pol data.

The REORDER software package developed at UCAR was used to convert raw S-Pol data to gridded data in Cartesian space at levels of constant height. The output of the REORDER software was then input to the CEDRIC software, which made it possible to examine the various temperature heights for each of the storms to determine the time-height trends of graupel-hail and ice crystals.

MATLAB was used to plot the time-height trends of reflectivity and plots of time vs. electric potential.

A detailed discussion of the methodology used to analyze various aspects of the thunderstorms is provided in the next chapter.

CHAPTER FOUR: METHODOLOGY

4.1: Finding storms using NEXRAD data

The S-Pol scanned a total of eight days over the KSC. NEXRAD level II data obtained from the National Climatic Data Center (NCDC) was processed and displayed for these days, using the WDSS-II software. The SCIT algorithm was then run on the processed data to obtain a list of storms that occurred over the KSC.

For this study, 10 storms that occurred over the KSC were considered. Six of these storms were CG lightning producing storms while four were non-CG lightning storms. Figures 4.1 and 4.2 show the locations of the CG lightning producing storms and non-CG storms respectively that were analyzed during the course of this project.

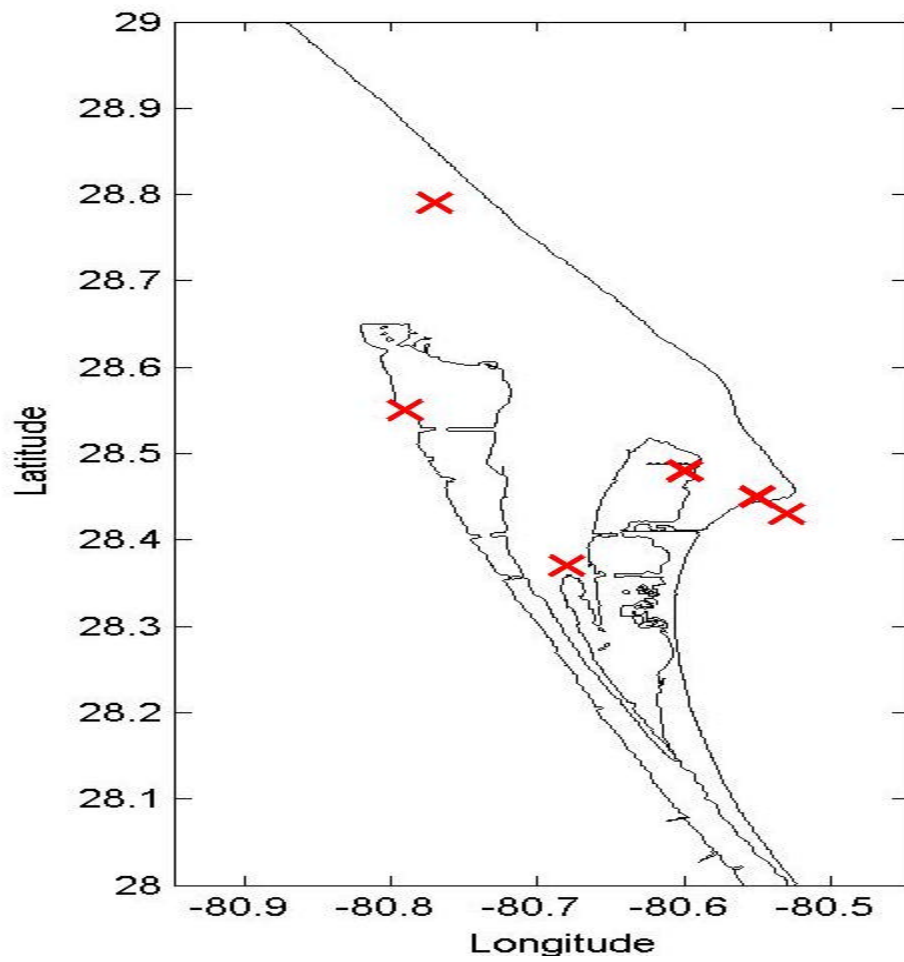


Figure 4.1: Location of CG Lightning producing storms

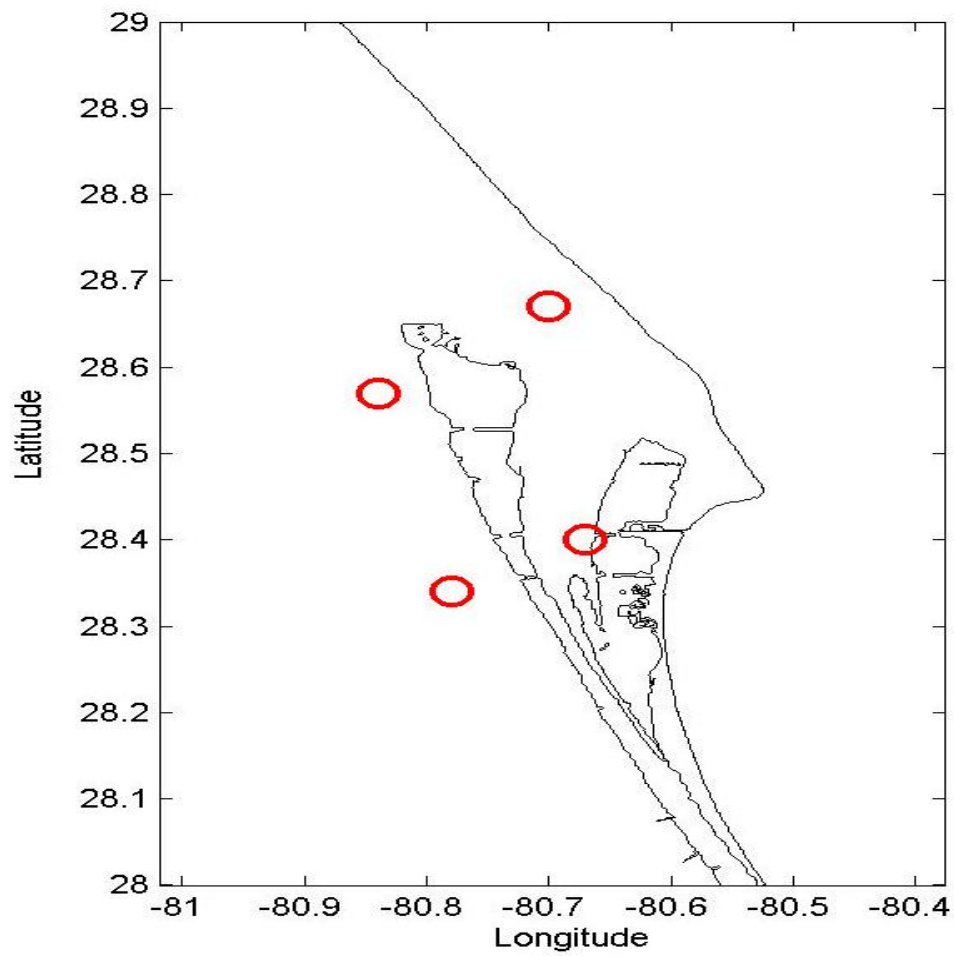


Figure 4.2: Location of non-CG Lightning storms

The SCIT algorithm can be applied to raw Nexrad data in order to identify storm cells. The algorithm defines a storm cell by processing reflectivity data for the NEXRAD in elevation and azimuth. First, all azimuth angles are considered for each and every elevation angle. A storm segment is identified as a set of contiguous range gates with reflectivity values greater than the specified threshold values of 30,35,40,45,50,55 and 60 dBz, and with a length greater than or equal to 1.9 km. Next, storm segments that are adjacent to each other- either overlapping or that lie in another azimuth but at a distance of less than 2 km are grouped together. Thus a storm cell is now defined in the azimuth. To define the storm cell in the elevation, i.e. to obtain height of the storm cell, centroids at adjacent elevation angles that are at a distance of approximately 5-10 km of each other are linked together. The centroid of the storm at a particular elevation angle is defined as the cell of maximum reflectivity at that elevation angle. The SCIT algorithm assigns a unique cell-identification number to each storm, and displays the attributes of each storm in the form of a table. Figure 4.3 shows the output of the SCIT algorithm when it is applied to Nexrad data.

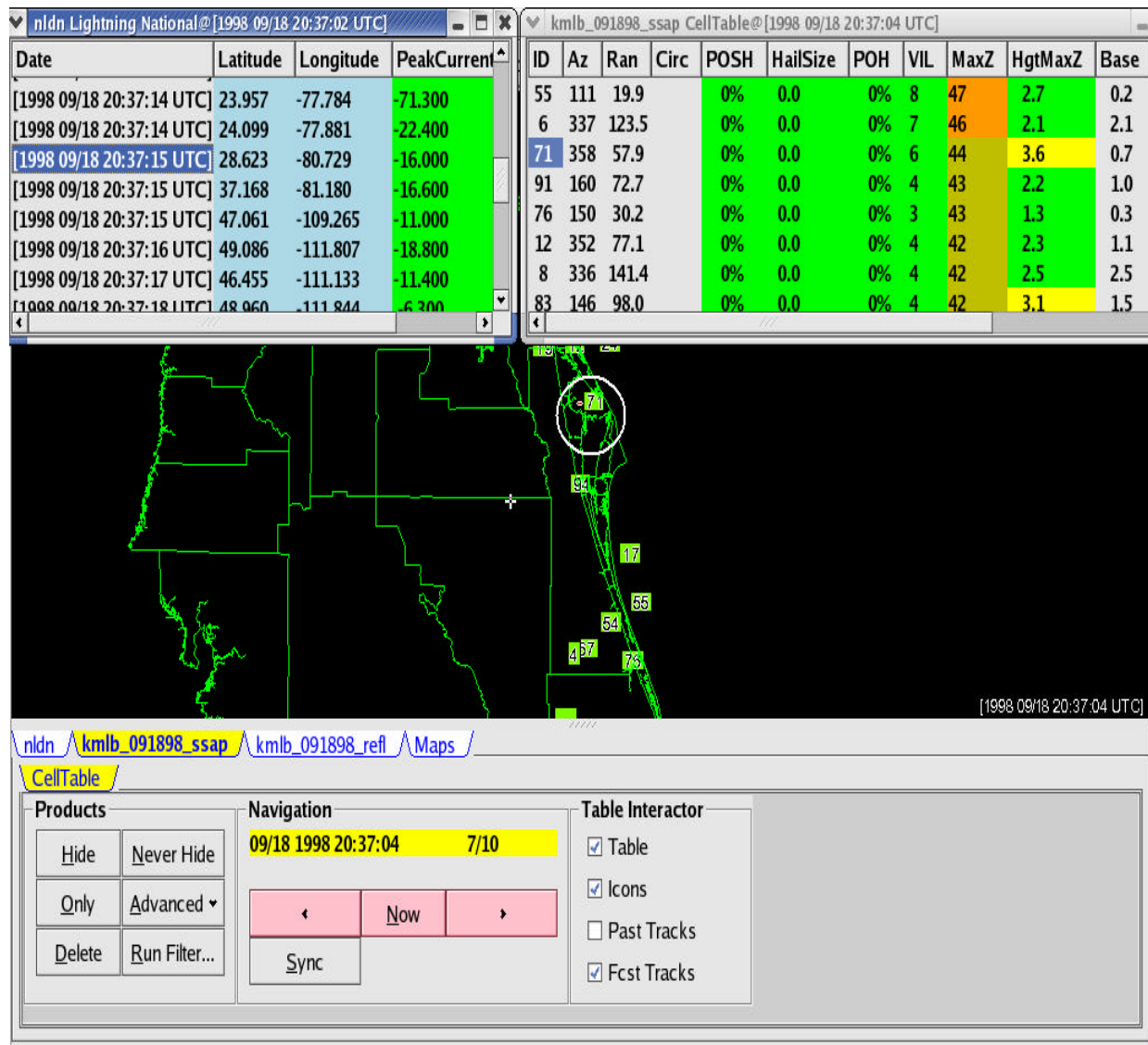


Figure 4.3: Output of the SCIT algorithm for Nexrad data

Having thus obtained the storms, it was necessary to overlay lightning data obtained from the NLDN onto the storm data to see if a storm produced lightning and if it did, when the first cloud-to-ground lightning flash occurred. A close-up of the circled portion from figure 4.3 is shown below in figure 4.4. This particular storm produced a negative cloud-to-ground lightning strike over the KSC as can be seen from the figure.



Figure 4.4- Lightning producing storm as obtained from Nexrad data

4.2: Locating a storm using S-POL data

Having located storms with cloud-to-ground lightning strikes over the KSC, the next step was to locate the same storm in the S-Pol data. This was done by laying both sets of data side-by-side and visually comparing the data. A group of storms as seen by the NEXRAD and the S-Pol is shown in figures 4.5 and 4.6 respectively.

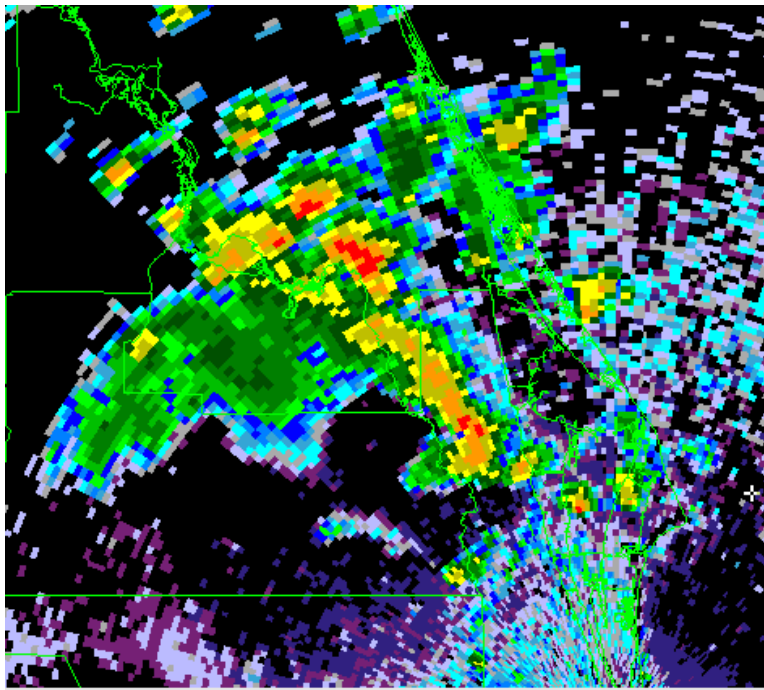


Figure 4.5- A set of storms as seen by the Nexrad

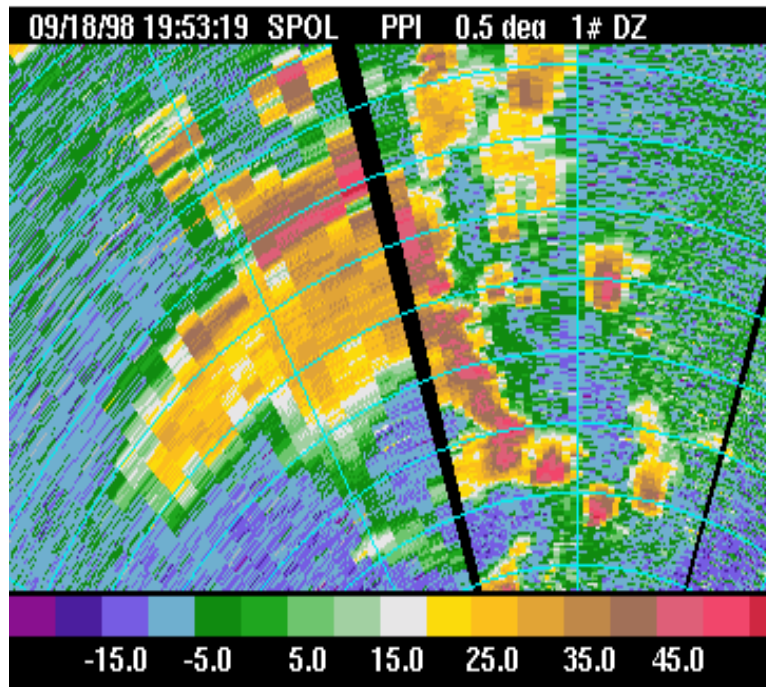


Figure 4.6- The set of storms in figure 4.1 as seen by the S-Pol

4.3: Plotting the time-height trends of ice, graupel and reflectivity

In order to plot time-height trends of reflectivity, the maximum reflectivity at each elevation angle for the storm was noted along with its height. These values were then gridded to a uniform grid using MATLAB. A resolution of 36 seconds on the time axis and 1 km on the height axis was chosen for the gridding. The cubic method of interpolation was used to grid the data. The

gridded values were then contoured using MATLAB once again to obtain a plot of time vs. height. A sample plot is shown below in figure 4.7

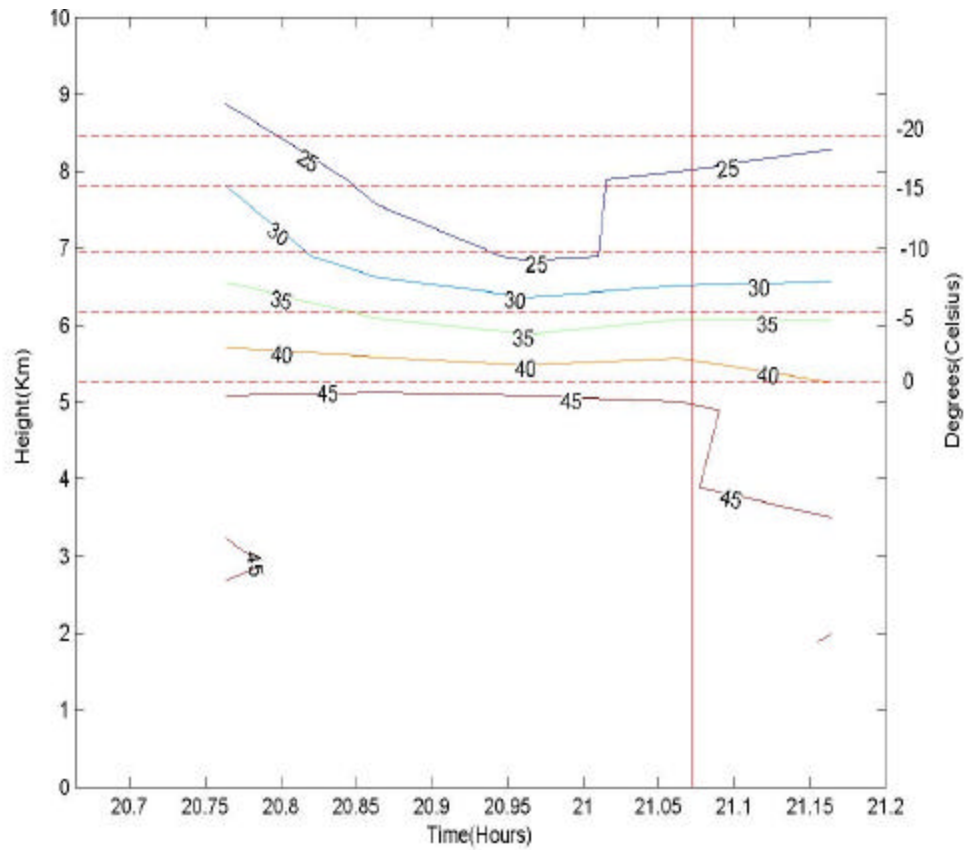


Figure 4.7: Time –Height reflectivity contour for a thunderstorm

The vertical line indicates the time of the 1st cloud-ground lightning strike while the horizontal lines indicate the locations of the various temperature isotherms. The determination of the sounding levels is explained later in the chapter.

In order to analyze the microphysical structure of the storm, a particle identification algorithm was run on the processed S-Pol data, in order to identify the hydrometeor types present in the thunderstorm cloud. The hydrometeor types considered for this analysis were graupel-hail and ice crystals.

The problem with plotting the time-height trends of hydrometeor types in same way that the reflectivity trends were plotted was that it was necessary to have a constant height for each measurement, which was not possible in this case because there was no “maximum” hydrometeor type that could be used as a sample point. Therefore, in order to determine the height for each hydrometeor measurement, the raw S-Pol data was first converted to Cartesian space from radar space using the REORDER software from UCAR, and then gridded to levels of constant height. The resolution chosen was 1 km each for the x-axis and y-axis, and 0.1 km for the z-axis. The reason for choosing such a small increment on the zaxis was to be able to observe the various temperature levels with greater accuracy. The gridded files output by the

REORDER software were then contoured and viewed using the CEDRIC software. For each storm, the various temperature levels were examined and the trends of graupel-hail and ice were observed. Thus it was possible to evaluate when the presence of ice or graupel-hail first occurred at a particular temperature level. A typical ice-graupel-hail plot is shown in figure 4.8.

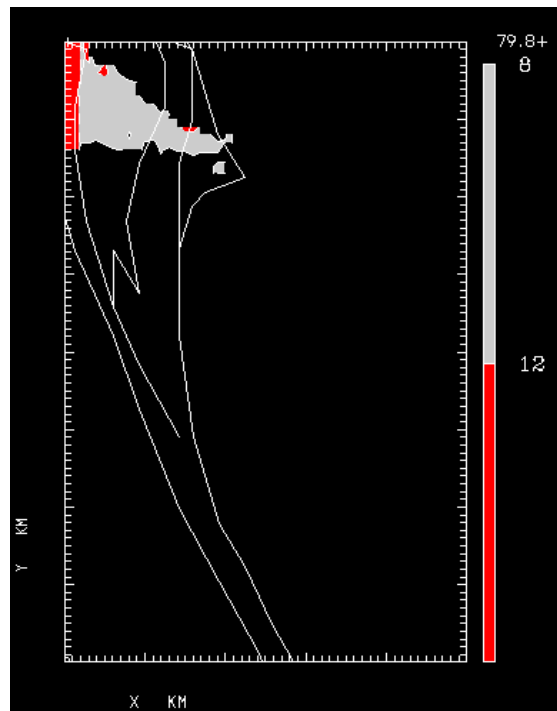


Figure 4.8: Graupel-hail-ice distribution within a thunderstorm

Figure 4.8 depicts the Florida coastline. The ice-graupel-hail distribution for a thunderstorm that occurred over the KSC has been overlaid onto the same plot. The red indicates presence of ice-crystals while the white indicates presence of graupel-hail. The x -axis and y-axis depict the distance in kilometers. The S-Pol is located at (0, 0) i.e. the left-bottom corner.

Having plotted the time-height trends of reflectivity, the next step was to overlay onto these plots the locations of the various temperature levels. These temperature levels were obtained by looking at sounding data obtained from balloon launches at the CCAS. The levels of interest were the 0,-5,-10,-15 and the -20 degree Celsius isotherms. In order to obtain the heights for these particular isotherms the raw balloon data was plotted in MATLAB and the values were interpolated to obtain the necessary heights. An example of the plotted sounding data is shown in Figure 4.9 below. The red points mark the levels of the 0,-5,-10,-15 and the -20 degree Celsius isotherms, as obtained by interpolation.

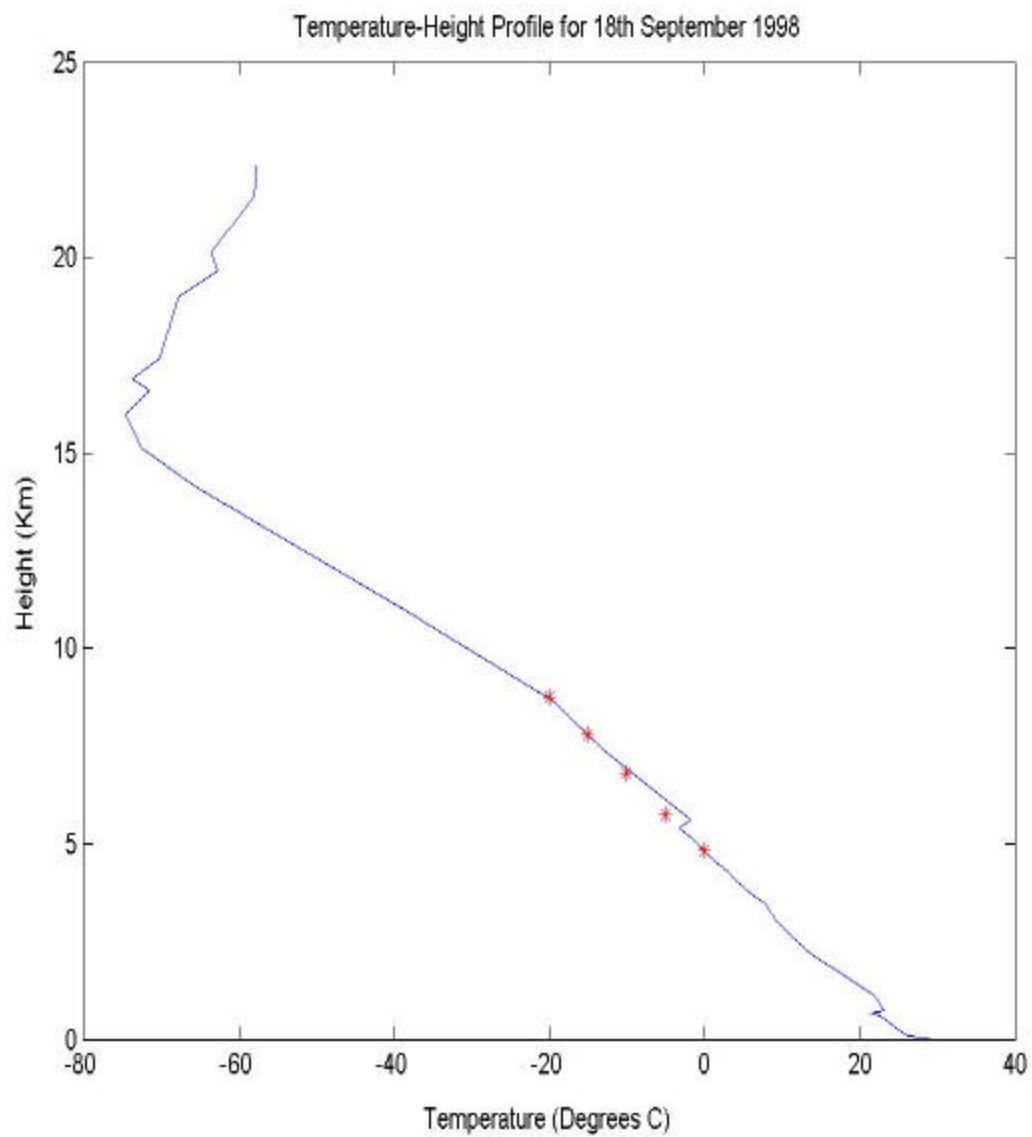


Figure 4.9- Sounding data obtained from balloon launches at the CCAFS

4.4: Electric Potential Trends of the Thunderstorms

Electric potential data obtained from the electric field-mill network at the KSC was plotted on a graph of time vs. electric potential for each thunderstorm. For each volume scan of the thunderstorm, the latitude and longitude of the centroid of the storm, or rather the range gate that the Nexrad identified as having the maximum reflectivity within that particular elevation angle was selected as a reference point for that storm. Having known the latitudes and longitudes of the electric field mills, the distance between the storm and each of the field mills was calculated.

In order to determine the closest field-mill to the storm, the storm location and each of the 34 field mill co-ordinates were first converted from spherical space to Cartesian space as shown in figure 4.10. Once the co-ordinates of both the storm and field-mills were determined in Cartesian space, the angle between each of the field-mills and the storm was calculated. This being done, the distance between each of the field-mills and the storm was calculated using the arc-length formula. The field-mill that gave the least distance value was selected as the field-mill closest to the storm. This procedure is explained in detail over the next few pages.

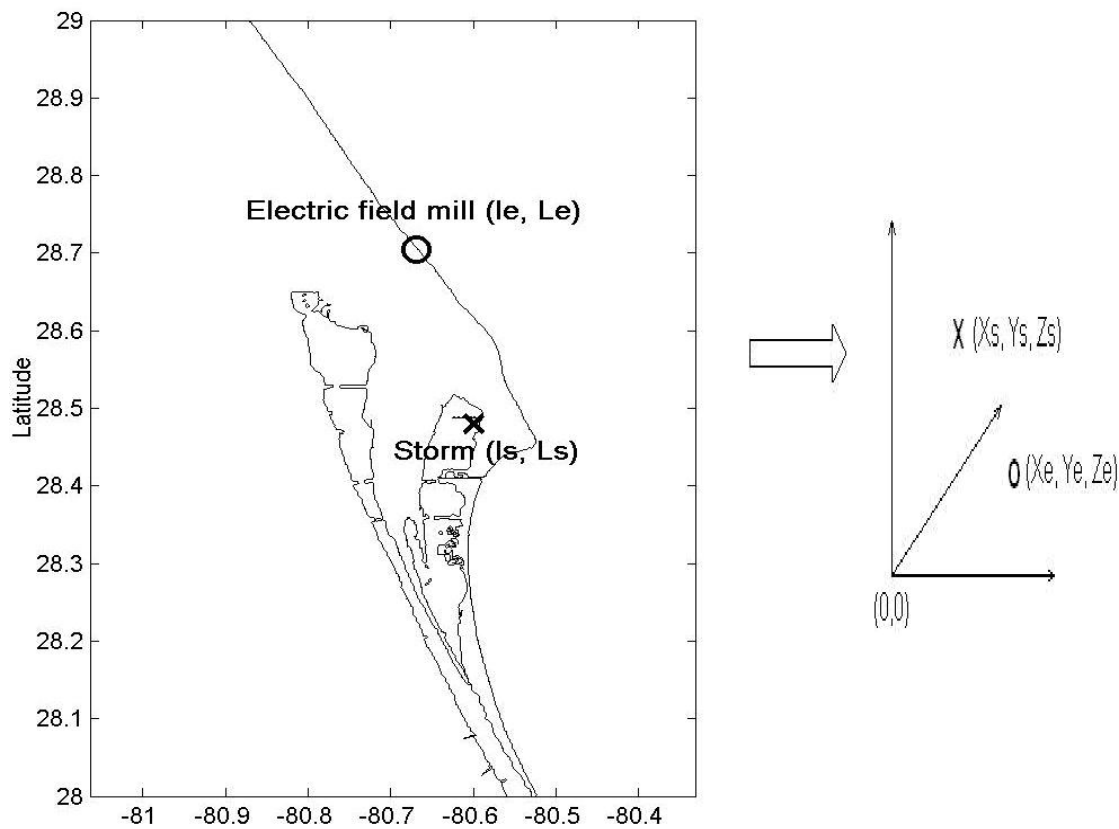


Figure 4.10: Conversion of co-ordinates from spherical to Cartesian space

With reference to figure 4.10. If we consider,

(l_s, L_s): (Longitude, Latitude) of the storm in spherical space.

(l_e, L_e): (Longitude, Latitude) of the electric field mill in spherical space,

$R = 6370$ km (Radius of the earth)

Then we have,

$$X_s = R * \cos(L_s) * \cos(l_s)$$

$$Y_s = R * \cos(L_s) * \sin(l_s)$$

$$Z_s = R * \sin(L_s)$$

$$X_e = R * \cos(L_e) * \cos(l_e)$$

$$Y_e = R * \cos(L_e) * \sin(l_e)$$

$$Z_e = R * \sin(L_e)$$

Having thus determined the location of the storm (X_s, Y_s, Z_s) and the location of the field- mill (X_e, Y_e, Z_e) in terms of a Cartesian co-ordinate system, with the center of the earth as the origin, the next step was to determine the angle between the two points subtended at the center of the earth. In order to accomplish this, the dot product of the two vectors formed by the points and the origin of the system, was determined, as shown in figure 4.11.

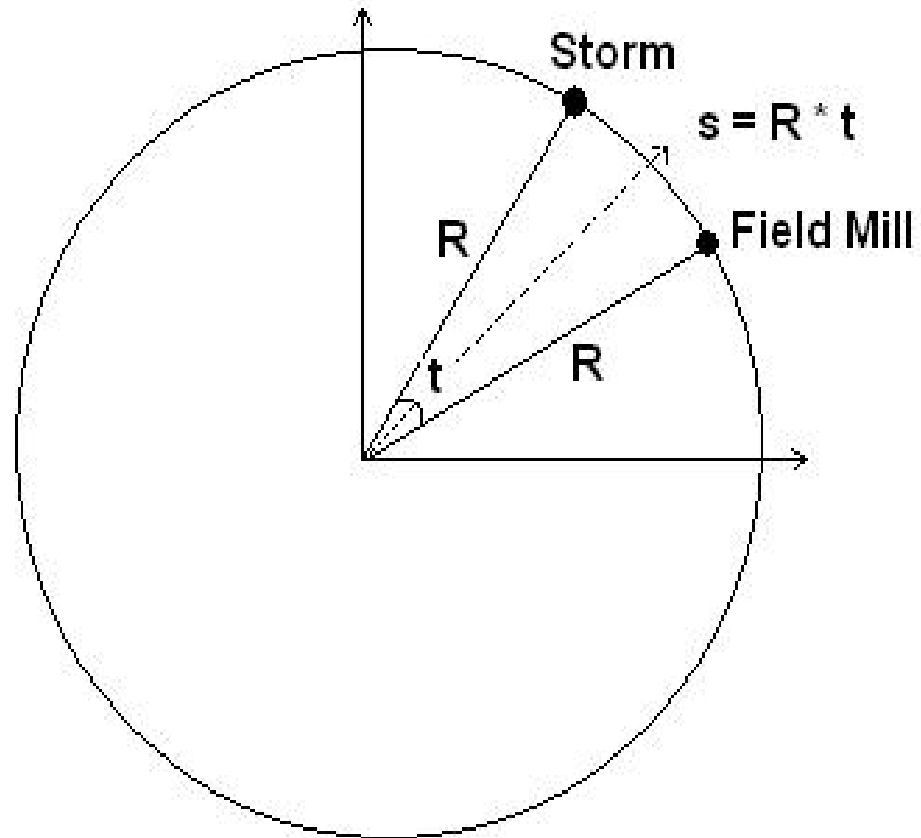


Figure 4.11: Determining the distance between the storm and field mill

Mathematically, the dot product between the two vectors can be stated as.

$$X_s * X_e + Y_s * Y_e + Z_s * Z_e = \cos(t),$$

Where, t is the angle between the vectors (X_s, Y_s, Z_s) and (X_e, Y_e, Z_e)

$$\text{Thus, } t = \cos^{-1}(X_s * X_e + Y_s * Y_e + Z_s * Z_e)$$

Using the formula arc length = Radius * angle,

$$\text{We have } S = R * t_{\text{radians}}$$

Thus the field mill closest to the storm was determined. The electric potential data for that particular volume scan was then taken from the selected field mill data file. The electric potential data for each thunderstorm was then put together and plotted on a graph of time (x-axis) vs. electric potential (y-axis). If the storm produced lightning, the location of the lightning strike was then overlaid onto this plot. A sample plot is shown below. The red vertical line indicates the time of the 1st cloud-ground lightning strike.

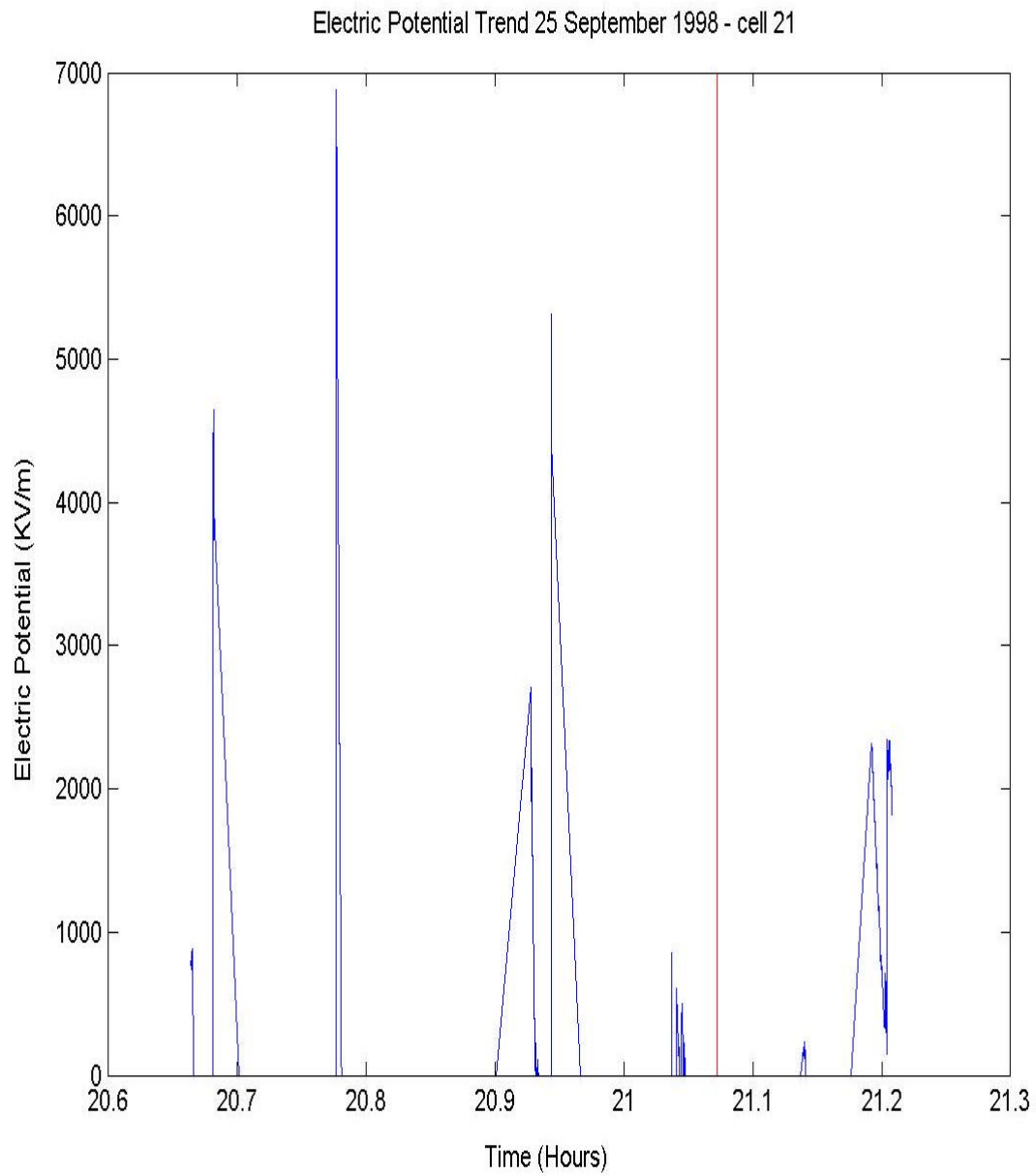


Figure 4.12: Electric Potential Trend of a thunderstorm

CHAPTER FIVE: OBSERVATIONS AND CONCLUSIONS

A total of 10 storms that occurred over the KSC were studied for this project. Of these, six storms produced cloud-ground lightning while four storms did not. Three aspects of each of the thunderstorms were analyzed for this project,

- ? Time vs. height trends of S-Pol reflectivity
- ? Time vs. electric potential trends for each of the thunderstorms
- ? Time vs. height trends of graupel – hail and ice

Having established some sort of forecasting signature from the above-mentioned trends, the efficiency of each of those signatures was calculated using parameters like the Probability of Detection (POD), the False Alarm Rate (FAR) and the Critical Success Index (CSI). These parameters are defined mathematically as follows,

If a = Total number of events that were forecast and were indeed observed,

If b = Total number of events that were forecast and but not observed,

If c = Total number of events that were not forecast but observed,

Then,

The Probability Of Detection (POD) is defined as $POD = a / (a+c)$

The False Alarm Rate (FAR) is defined as $FAR = b / (a+b)$

The Critical Success Index is defined as $CSI = a / (a+b+c)$

We now discuss each of the aspects analyzed in detail in the following sections.

5.1: Forecasting Signatures from Reflectivity

For each of the storms, having plotted the time –height trends of reflectivity, the 35 dBz, 40 dBz and 45 dBz echoes at the 0°C, -5°C and -10°C temperature levels were analyzed. The basic idea was to establish a trend that was consistent in all cloud-ground lightning producing storms, but at the same time that was not present in the non lightning storms. Once this was done, and such a trend was obtained, its efficiency was calculated using the parameters discussed previously. A lightning signature was deemed to be the existence of a particular reflectivity echo above a particular temperature level for two consecutive volume scans of the S-Pol. Since a typical volume scan for the S-Pol takes approximately 2.5 minutes with a gap of a minute between each scan, the signature had to exist for at least 6 minutes before it could be considered as valid. The results obtained from this analysis are tabulated in the tables below.

The tables below show the forecasting matrix for lightning and non-lightning producing storms. A Yes/No (1/0) scheme is used to depict whether the required condition was met or not. The a, b, and c values are computed from these tables to further determine the POD, FAR and the CSI. Storms 1-6 are lightning producing storms while storms 7-10 are non-lightning producing ones.

Table 5.1: Forecasting Matrix for the 35 dBz echo existing at the 0°C level

	Storm 1	Storm 2	Storm 3	Storm 4	Storm 5	Storm 6	Storm 7	Storm 8	Storm 9	Storm 10
35 dBz > 0°C level	1	1	1	1	1	1	1	1	1	1

From the above table, the values of a, b and c can be calculated to be, a= 6, b=4 and c=0

Thus, for this signature the POD = 60%, the FAR = 40% and the CSI = 60%.

Table 5.2: Forecasting Matrix for the 35 dBz echo existing at the -5°C level

	Storm 1	Storm 2	Storm 3	Storm 4	Storm 5	Storm 6	Storm 7	Storm 8	Storm 9	Storm 10
35dBz >-5°C level	1	1	1	1	1	1	0	0	1	0

From table 5.2, the values of a, b and c can be calculated to be, a=9, b=1, and c=1. Thus, for this signature the POD = 90%, the FAR = 10% and the CSI =81.8%.

Table 5.3: Forecasting Matrix for the 35 dBz echo existing at the -10°C level

	Storm 1	Storm 2	Storm 3	Storm 4	Storm 5	Storm 6	Storm 7	Storm 8	Storm 9	Storm 10
35dBz > -10°C level	1	1	1	0	0	1	0	0	0	0

From table 5.3, the values of a, b and c can be calculated to be, a= 8, b=2 and c=2

Thus, for this signature the POD = 80%, the FAR = 20% and the CSI = 66.67%.

Table 5.4: Forecasting Matrix for the 40 dBz echo existing at the 0°C level

	Storm 1	Storm 2	Storm 3	Storm 4	Storm 5	Storm 6	Storm 7	Storm 8	Storm 9	Storm 10
40dBz > 0°C level	1	1	1	1	1	1	1	1	1	0

From table 5.4, the values of a, b and c can be calculated to be, a= 7, b=3 and c=3

Thus, for this signature the POD = 70%, the FAR = 30% and the CSI = 53.8%.

Table 5.5: Forecasting Matrix for the 40 dBz echo existing at the -5°C level.

	Storm 1	Storm 2	Storm 3	Storm 4	Storm 5	Storm 6	Storm 7	Storm 8	Storm 9	Storm 10
40 dBz > -5°C level	1	1	1	1	1	0	0	0	0	0

From table 5.5, the values of a, b and c can be calculated to be, a=9, b=1, and c=1. Thus, for this signature the POD = 90%, the FAR = 10% and the CSI =81.8%.

Table 5.6: Forecasting Matrix for the 40 dBz echo existing at the -10°C level

	Storm 1	Storm 2	Storm 3	Storm 4	Storm 5	Storm 6	Storm 7	Storm 8	Storm 9	Storm 10
40 dBz > -10°C level	1	0	0	0	0	0	0	0	0	0

From table 5.6, the values of a, b and c can be calculated to be, $a=5$, $b=5$ and $c=5$

Thus, for this signature the $POD = 50\%$, the $FAR = 50\%$ and the $CSI = 33.33\%$.

Table 5.7: Forecasting Matrix for the 45 dBz echo existing at the $0^{\circ}C$ level

	Storm 1	Storm 2	Storm 3	Storm 4	Storm 5	Storm 6	Storm 7	Storm 8	Storm 9	Storm 10
45 dBz > $0^{\circ}C$ level	1	1	1	1	0	0	0	0	0	0

From table 5.7, the values of a, b and c can be calculated to be, $a=8$, $b=2$ and $c=2$

Thus, for this signature the $POD = 80\%$, the $FAR = 20\%$ and the $CSI = 66.67\%$.

Table 5.8: Forecasting Matrix for the 45 dBz echo existing at the $-5^{\circ}C$ level

	Storm 1	Storm 2	Storm 3	Storm 4	Storm 5	Storm 6	Storm 7	Storm 8	Storm 9	Storm 10
45 dBz > $-5^{\circ}C$ level	1	0	0	0	0	0	0	0	0	0

From table 5.8, the values of a, b and c can be calculated to be, $a=5$, $b=5$, and $c=5$. Thus, for this signature the $POD = 50\%$, the $FAR = 50\%$ and the $CSI = 33.3\%$.

Table 5.9: Forecasting Matrix for the 45 dBz echo existing at the -10°C level.

	Storm 1	Storm 2	Storm 3	Storm 4	Storm 5	Storm 6	Storm 7	Storm 8	Storm 9	Storm 10
45 dBz > -10°C level	1	0	0	0	0	0	0	0	0	0

From table 5.9, the values of a, b and c can be calculated to be, $a=5$, $b=5$ and $c=5$

Thus, for this signature the $POD = 50\%$, the $FAR = 50\%$ and the $CSI = 33.33\%$.

The next table combines all of the results obtained above. From this table it is now possible to establish the best signature in order to predict the onset of cloud-ground lightning in a thunderstorm. If the statistics of two or more signatures match exactly, then the time difference between the occurrence of the signature and the occurrence of the 1st cloud-ground lightning strike is used as a deciding factor.

Table 5.10: POD, FAR and the CSI for each reflectivity lightning signature

	POD (%)	FAR (%)	CSI (%)
35 dBz>0°C	60	40	60
35 dBz>-5°C	90	10	81.8
35 dBz>-10°C	80	20	66.67
40 dBz>0°C	70	30	53.8
40 dBz>-5°C	90	10	81.8
40 dBz>-10°C	50	50	33.33
45 dBz>0°C	80	20	66.67
45 dBz>-5°C	50	50	33.33
45 dBz>-10°C	50	50	33.33

From the above table, we can see that both the 35 dBz and the 40 dBz at the -5°C temperature level give the best statistics with a high POD of 90%, a low FAR of 10% and a high CSI of 81.8%. We now look at the time difference between the occurrence of the signature and the 1st cloud-ground lightning strike to determine the better of the two signatures. The average time difference between the occurrence of the 35 dBz signature and the 1st cloud-ground lightning strike was found to be approximately 22 minutes while the time difference for the 40dBz echo was found to be approximately 16 minutes. Hence, we can conclude that the occurrence of the 35 dBz echo at the -5 °C temperature level is the best indicator of imminent cloud-ground lightning, since there is more time between the occurrence of the signature and the occurrence of the first cloud-ground lightning strike.

5.2: Forecasting Signatures from Electric Potential

From the analysis of electric potential trends for each of the thunderstorms, it was observed that there was almost always a sudden surge in the electric potential to a value of approximately 1000 V/m approximately 15-25 minutes before the 1st cloud–ground lightning strike. This surge was observed mostly in cloud-ground lightning producing storms. Only one non cloud-ground lightning producing storm produced this surge. However since electric potential data for only seven out of ten storms was available for analysis, and because this trend was observed in six out of seven storms, not much comment can be made about the reliability of this phenomenon. Nonetheless, if treated as a signature this trend would give a POD of 83.3%, an FAR of 16.6% and a CSI of 71.42%.

5.3 Forecasting Signatures from Graupel-Hail and Ice Trends

The advantage of viewing a thunderstorm with the help of a dual-polarization radar like the S-Pol was that the microphysical structure of the storm could be analyzed. As stated in chapter four, ice and graupel-hail trends of time vs. height were plotted and analyzed. The 0°, -5° and -10° Celsius temperature levels were analyzed for each and every thunderstorm. No significant trend suggested itself during the analysis of the 0° and -5° temperature levels, but during the analysis of the -10° temperature level, it was observed that all the thunderstorms that went on to produce cloud-ground lightning had a significantly larger amount of graupel-hail present at this temperature level, than the storms that did not produce any cloud-ground lightning. The images of the graupel-hail-ice distribution are presented in the appendix.

5.4: Future Work

This section talks about a few ideas that could be investigated in order to come up with better signatures in order to forecast the onset of cloud-ground lightning in the future.

Currently, most signatures that predict lightning are based on reflectivity thresholds. The dual-polarization radar however, has made it possible to gain an insight into the microphysical structure of a storm. This thesis investigates the presence of ice and graupel-hail at the various temperature levels but indicates a signature merely in terms of presence or absence of graupel and ice at the various temperature isotherms. An actual quantitative threshold in terms of the volume of the graupel and ice at a particular temperature level perhaps, would prove to be a significantly better indicator of cloud-ground lightning.

Another aspect worth examining would be the occurrence of the last cloud-ground strike within a thunderstorm. Current research is bent on determining when the 1st cloud-ground lightning strike will occur, so necessary steps can be taken to preserve life and property. In the case of organizations like the KSC, it would be prudent to have an idea of how long the storm would produce lightning, so as to issue the lightning warning accordingly.

Lastly, an analysis of the onset of the first cloud-cloud lightning might prove invaluable in determining the time of the 1st cloud-ground lightning strike, since cloud-cloud lightning always occurs before a cloud-ground lightning strike.

APPENDIX
DETAILED STORM ANALYSIS

This appendix presents the time-height diagrams and electric-potential trend diagrams for a single CG lightning producing storm and a non CG lightning storm analyzed during the course of this study. Screen-shots of the storm as seen by the Nexrad are presented here, along with the time-height trends of reflectivity and hydrometeor types. Electric potential trend diagrams for the storms are also provided. Statistics for each storm like the start and end time (in UTC), type (lightning producing or non-lightning producing), time and location of the first cloud–ground lightning strike along with a brief description of the storm itself are mentioned.

A.1: 19 September 1998 (Cell 92) – storm #1

This lightning producing storm was detected by the Nexrad at 18:55:08 just south of the KSC. It later moved upwards and over the KSC where it produced its 1st negative cloud-lightning strike at 19:36:32, the location of the strike being 28.61N, 80.54W. A little after this it merged with two other systems just to its north. This combined system then went on to produce more cloud-ground lightning. All strikes produced by this storm, even after it merged with the other systems were negative in polarity. The sounding data for this storm revealed the 0°C, -5°C, -10°C, -15°C and the -20°C temperature levels to be at 5.0795 km, 6.0012 km , 7.0431 km, 7.7984 km and 8.6406 km above Mean Sea-Level respectively.

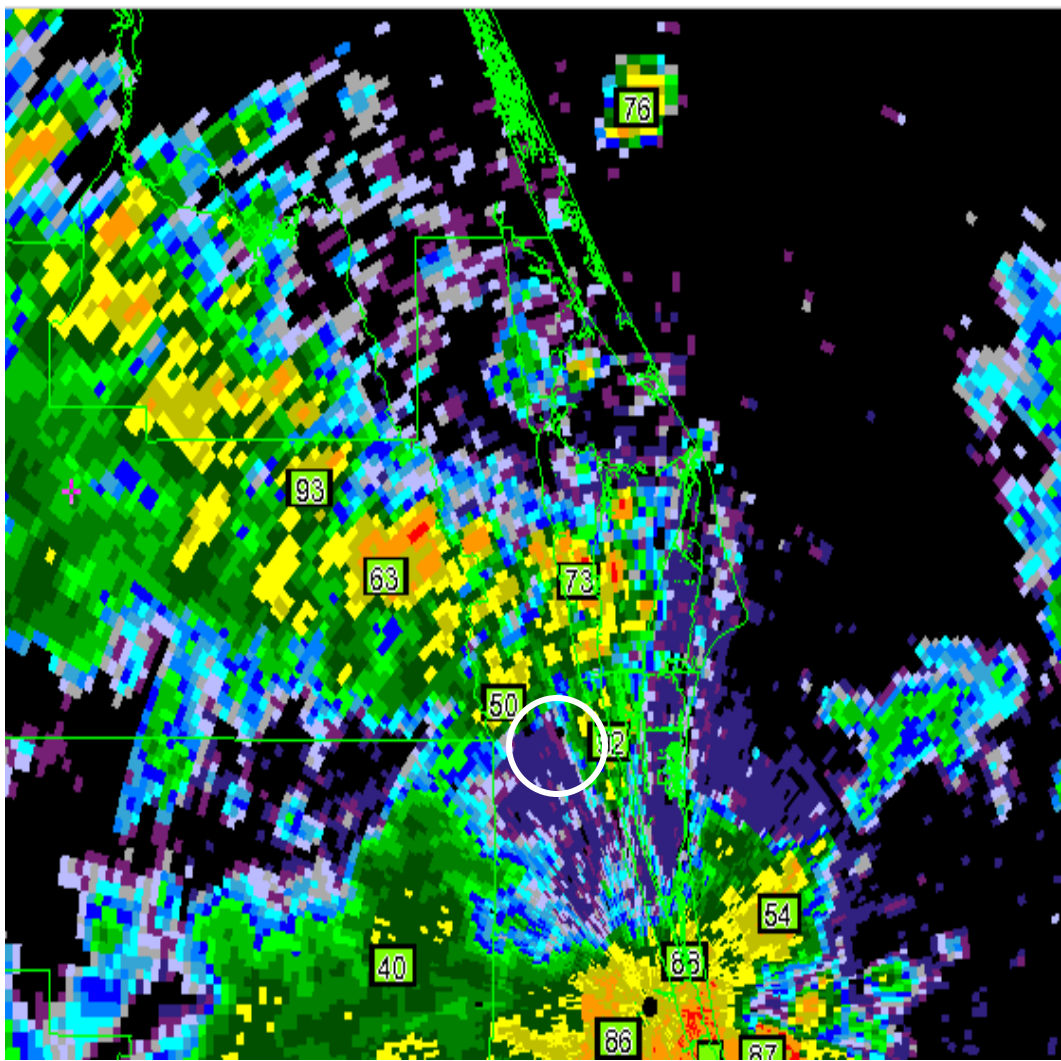


Figure A. 1: Storm#1 as seen by the Nexrad

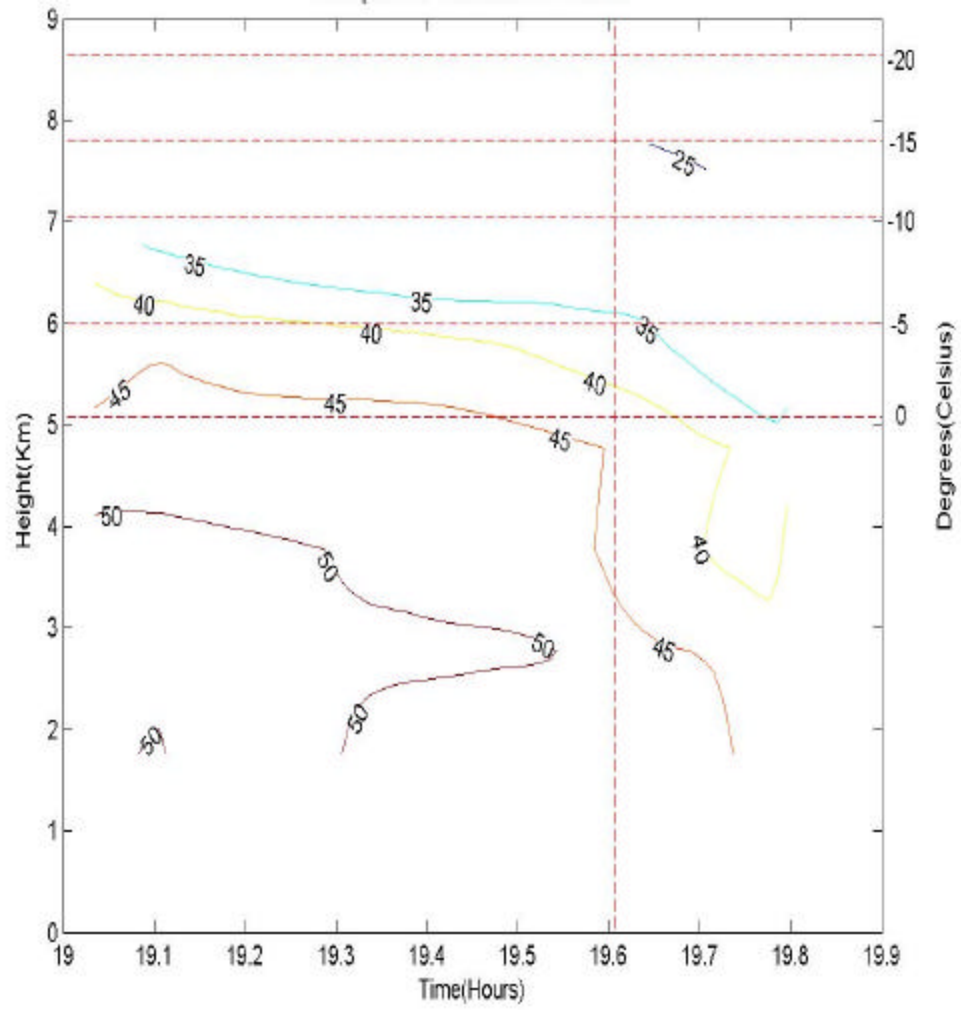


Figure A.2: Time vs. Height reflectivity trend for storm #1

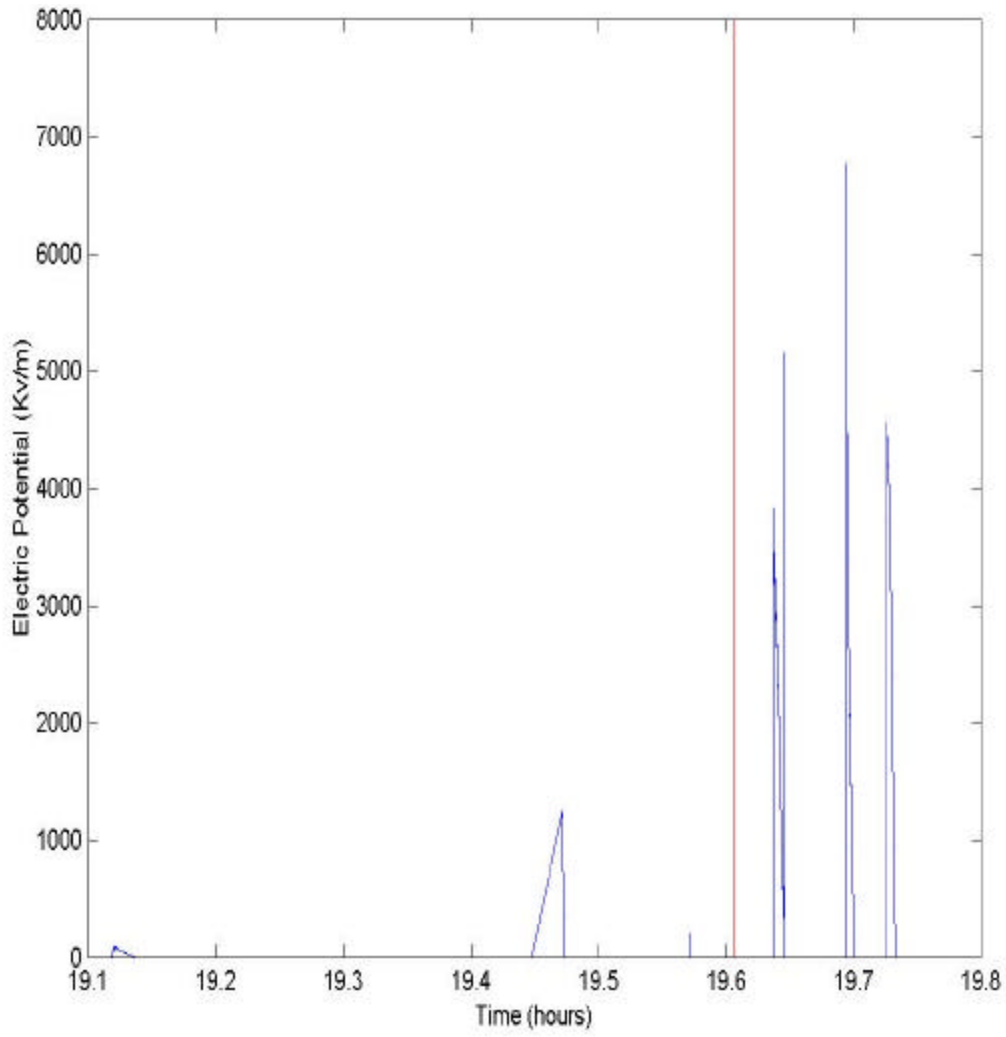


Figure A.3: Time vs. Electric Potential trend for storm #1

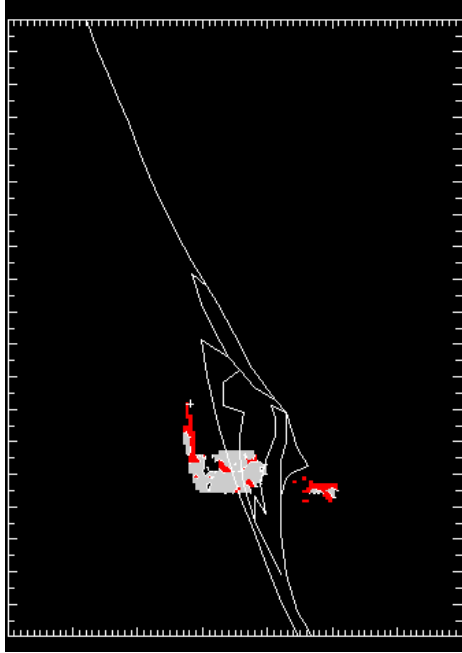


Figure A.4 (a): 0° C level at 18:55:39

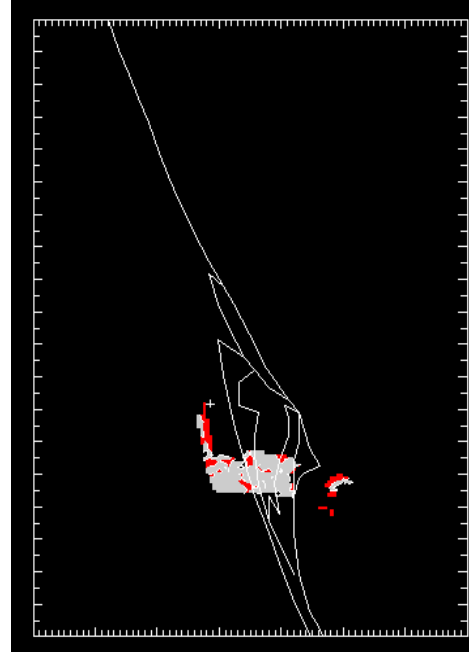


Figure A.4 (b): 0° C level at 19:01:36



Figure A.4 (c): 0° C level at 19:07:04

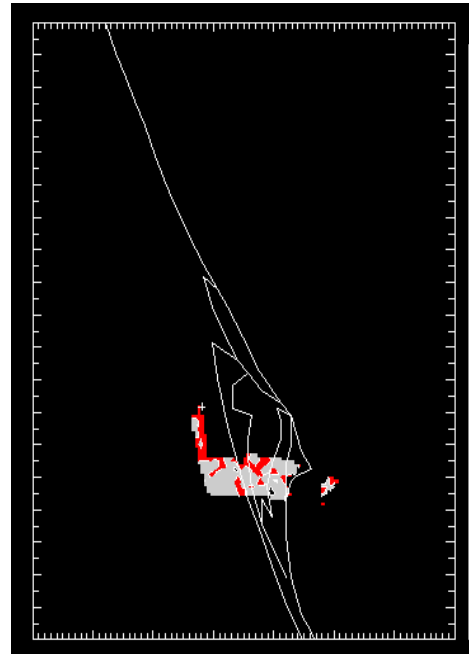


Figure A.4 (d): 0° C level at 19:12:32

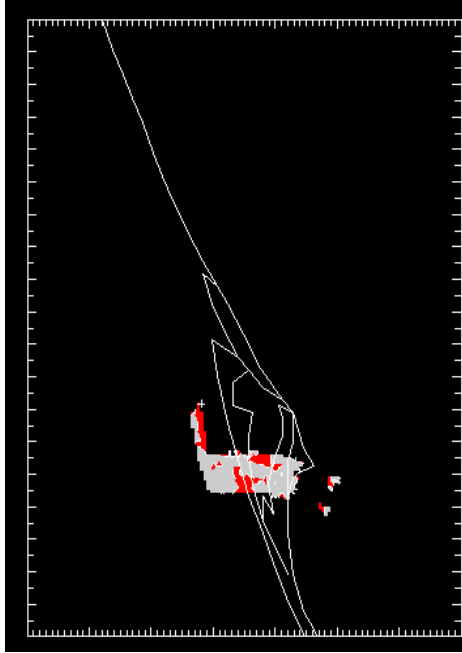


Figure A.4 (e): 0° C level at 19:18:00

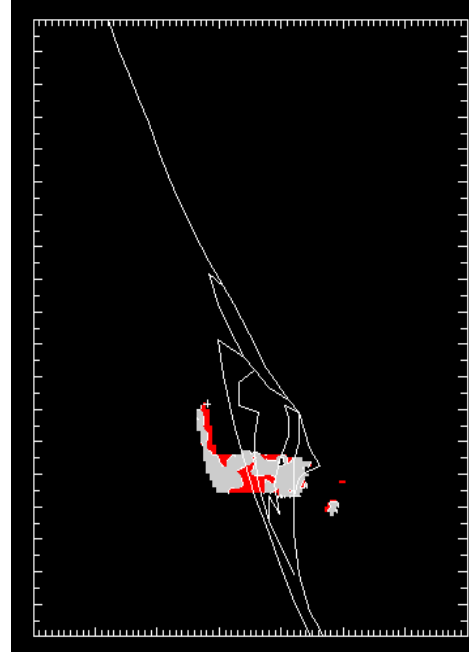


Figure A.4 (f): 0° C level at 19:23:28

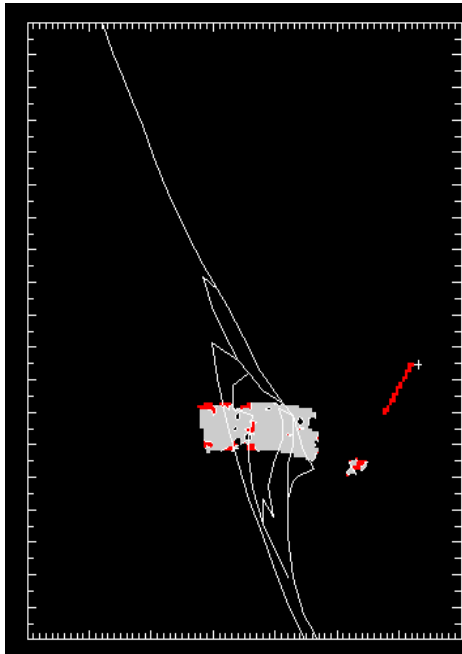


Figure A.4 (g): 0° C level at 19:28:49

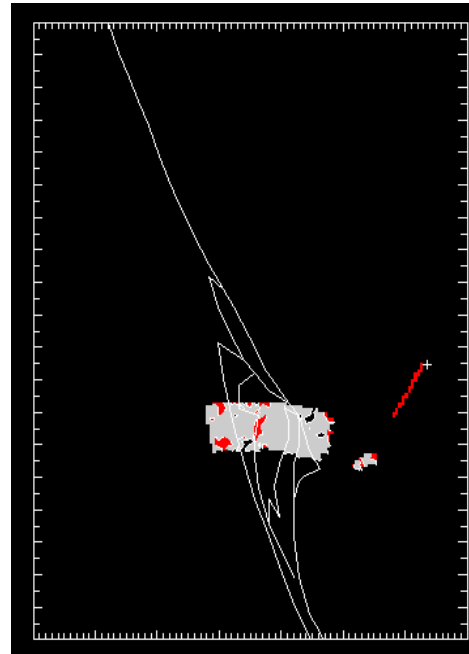


Figure A.4 (h): 0° C level at 19:34:17

Figure A.4: Ice-graupel-hail trends at the 0° C level for storm #1

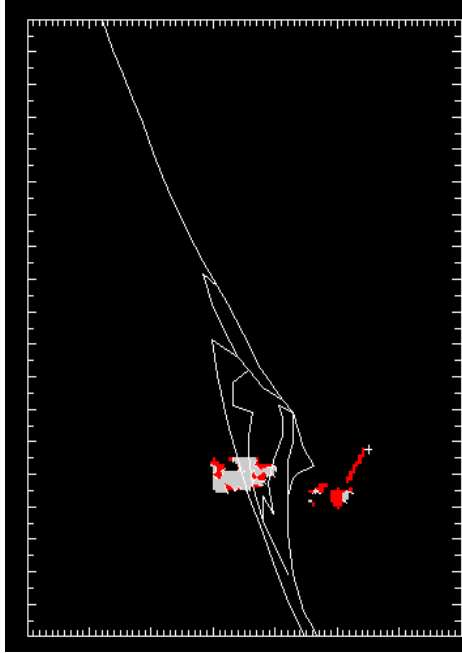


Figure A.5 (a): -5° C level at 18:55:46

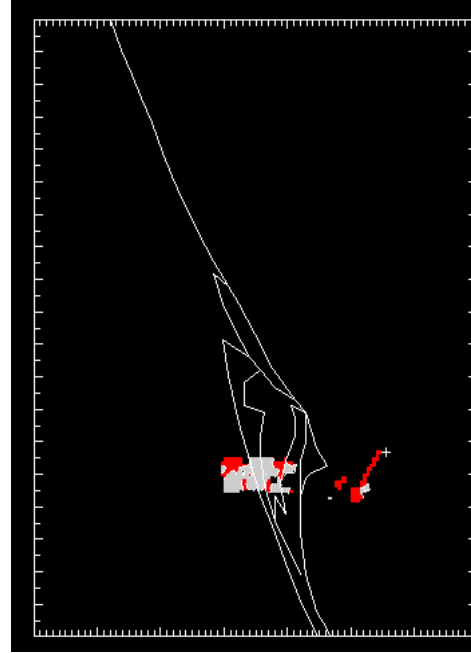


Figure A.5 (b): -5° C level at 19:01:43

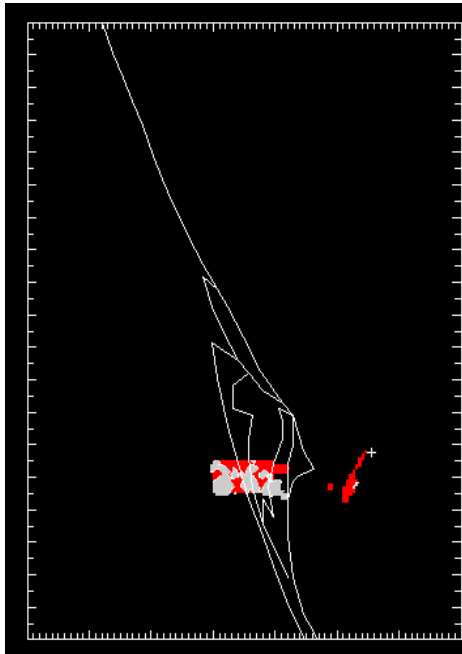


Figure A.5 (c): -5° C level at 19:07:11

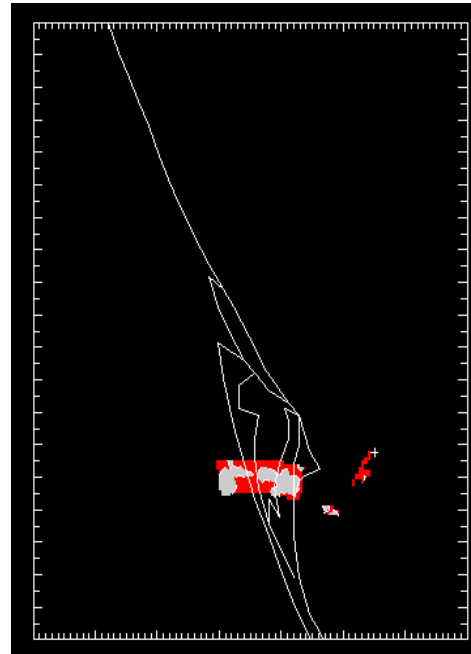


Figure A.5 (d): -5° C level at 19:12:11

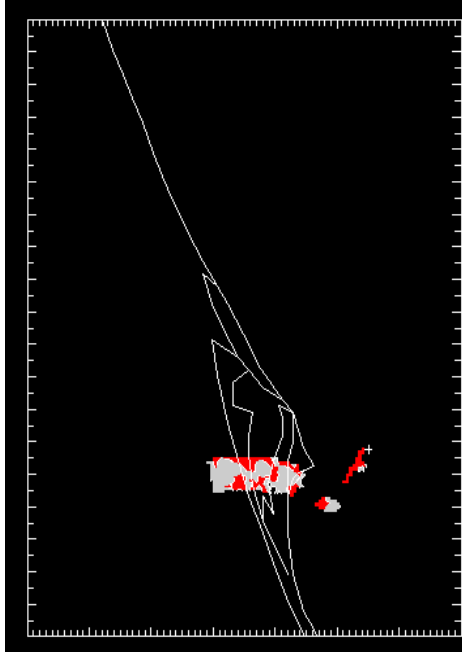


Figure A.5 (e): -5° C level at 19:23:35

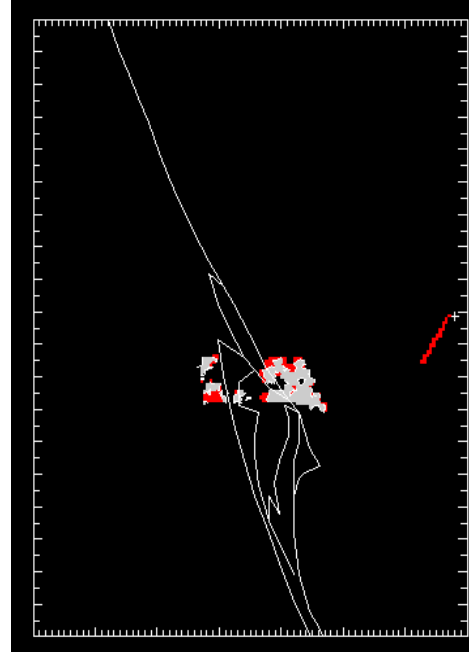


Figure A.5 (f): -5° C level at 19:28:56

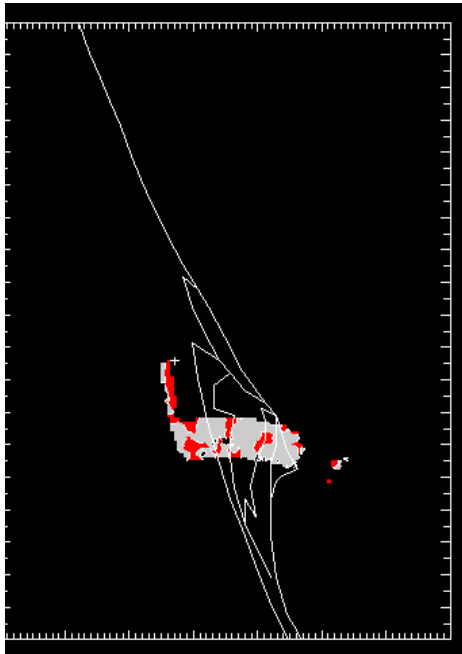


Figure A.5 (g): -5° C level at 19:34:17

Figure A.5: Ice-graupel-hail trends at the -5° C level for storm #1

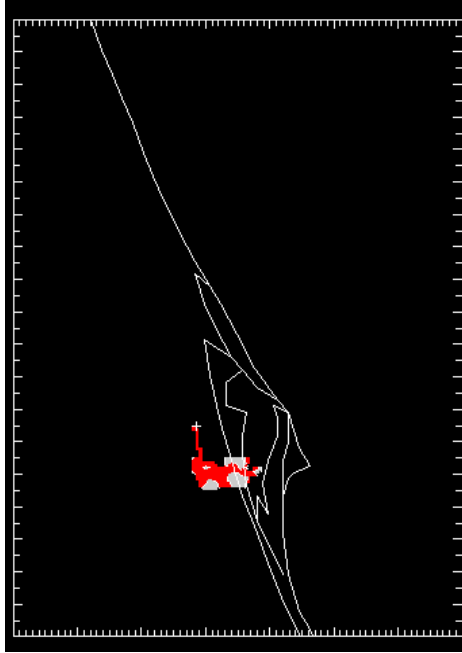


Figure A.6 (a): -10° C level at 18:55:53

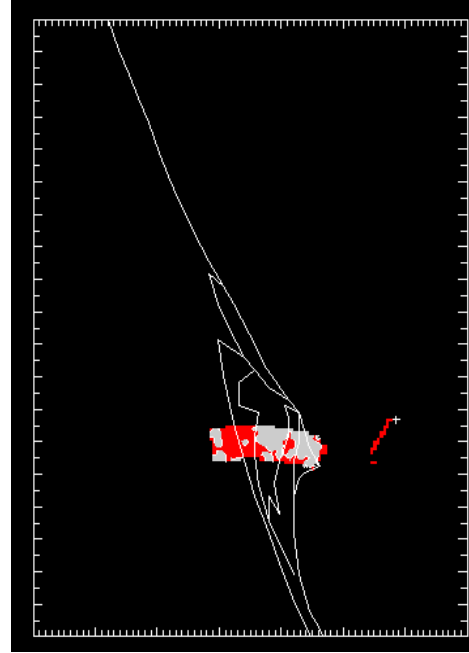


Figure A.6 (b): -10° C level at 19:01:51

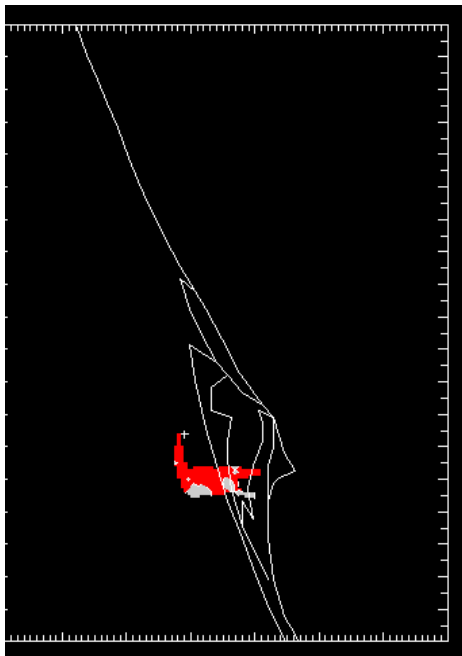


Figure A.6 (c): -10° C level at 19:18:14

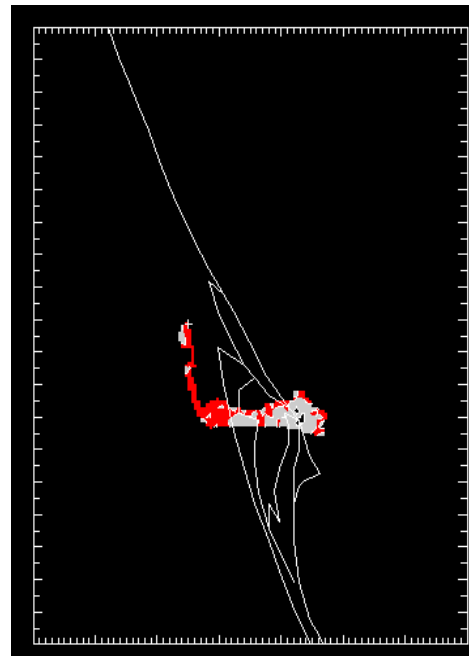


Figure A.5 (d): -10° C level at 19:23:43

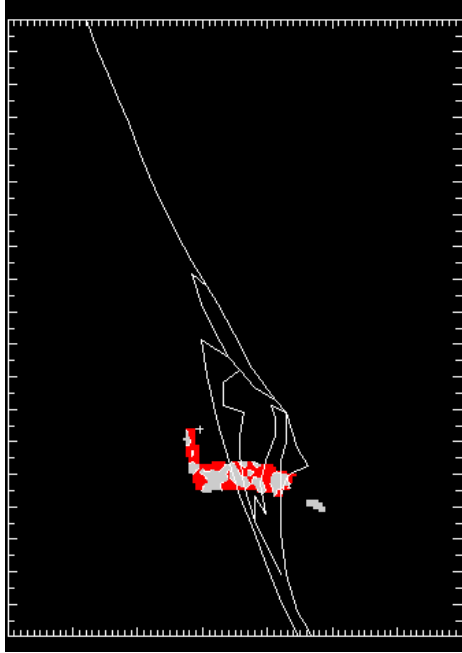


Figure A.6 (e): -10° C level at 19:29:03

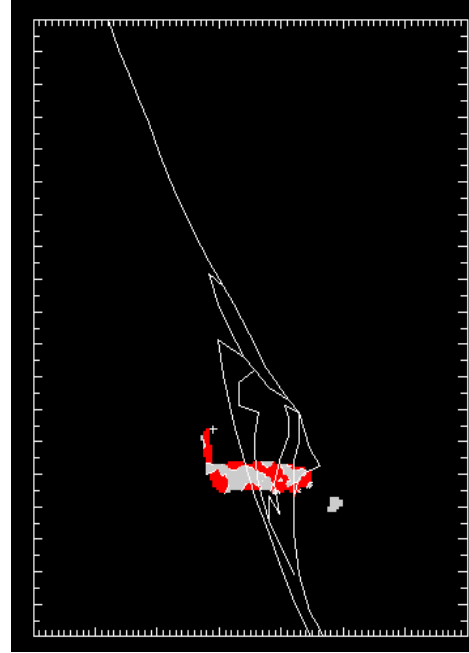


Figure A.6 (f): -10° C level at 19:34:24

Figure A.6: Ice-graupel-hail trends at the -10° C level for storm #1

A.2: 26 September 1998 (Cell 75) – storm #2

This isolated storm began at 16:29:16 and ended at 16:49:14. Of all the storms analyzed, it had the shortest duration. It did not produce any sort of lightning. It formed to the north of the KSC and moved further north before dissipating. The 0°C, -5°C, -10°C, -15°C and the -20°C temperature isotherms for the storm as observed from the balloon sounding were located at 4.7954 km, 5.9873 km, 6.9883 km, 7.5675 km and 8.1129 km respectively. No reflectivity levels greater than 45 dBz were observed during this storm. Electrical potential trends did not indicate any values greater than 0 V/m.

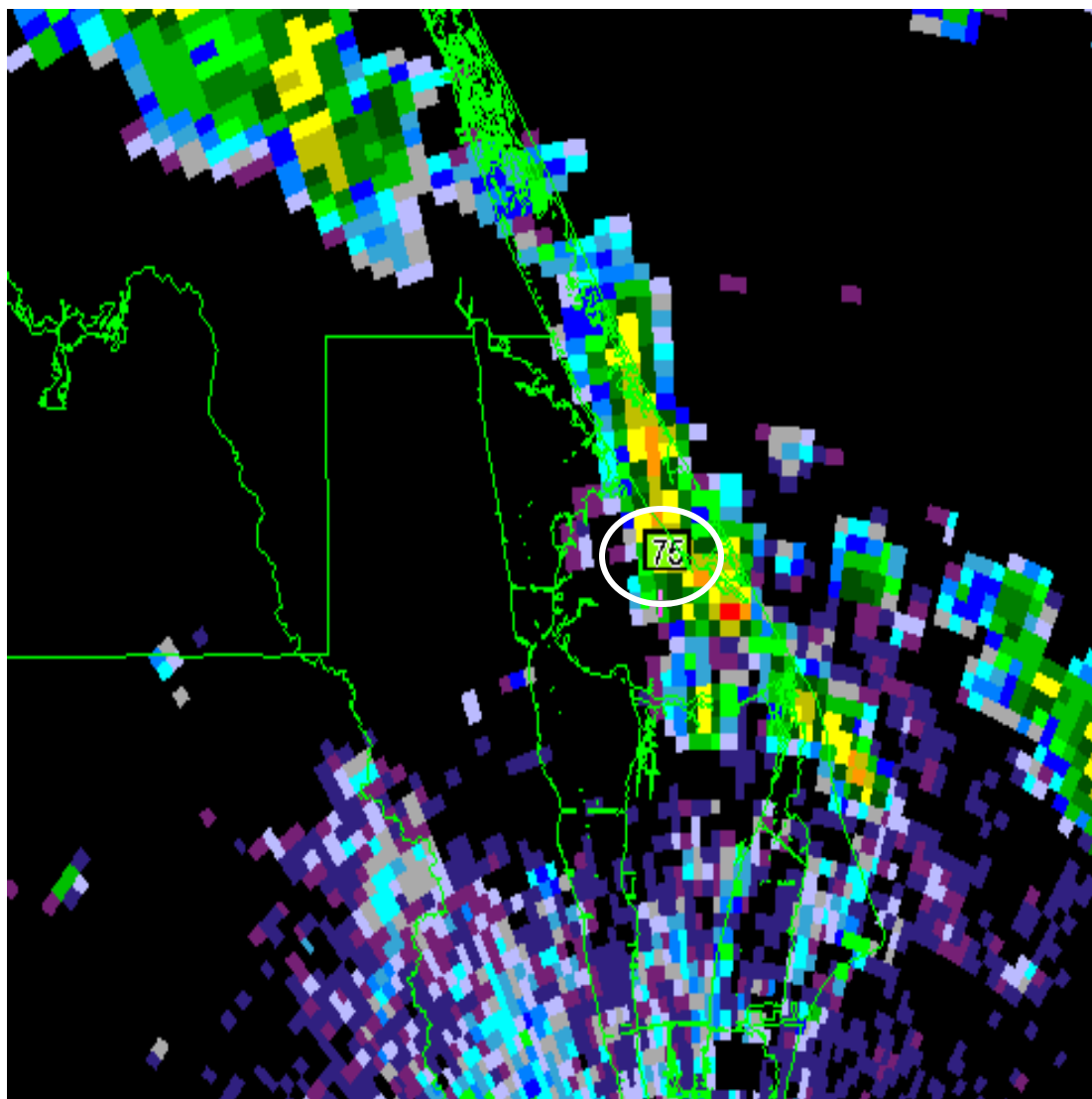


Figure A.7: Storm #2 as seen by the Nexrad

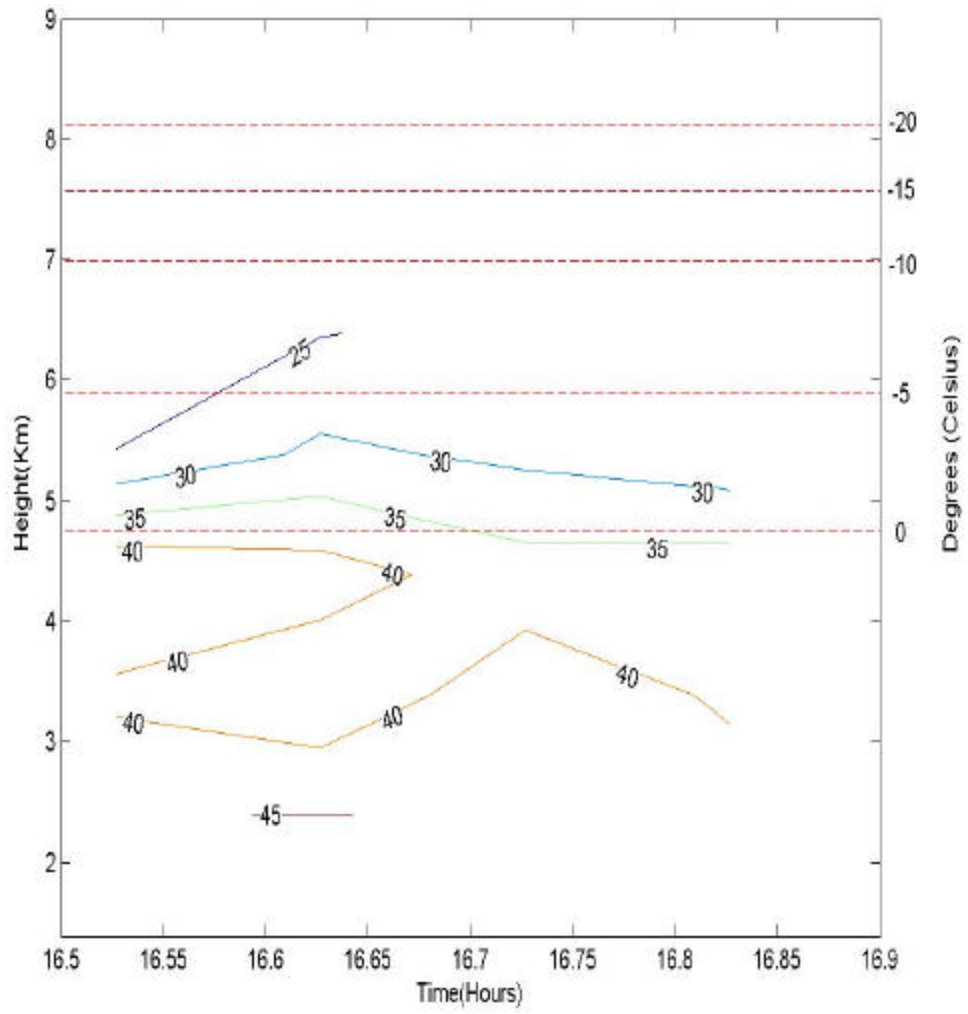


Figure A.8: Time vs. Height reflectivity trend for storm #2

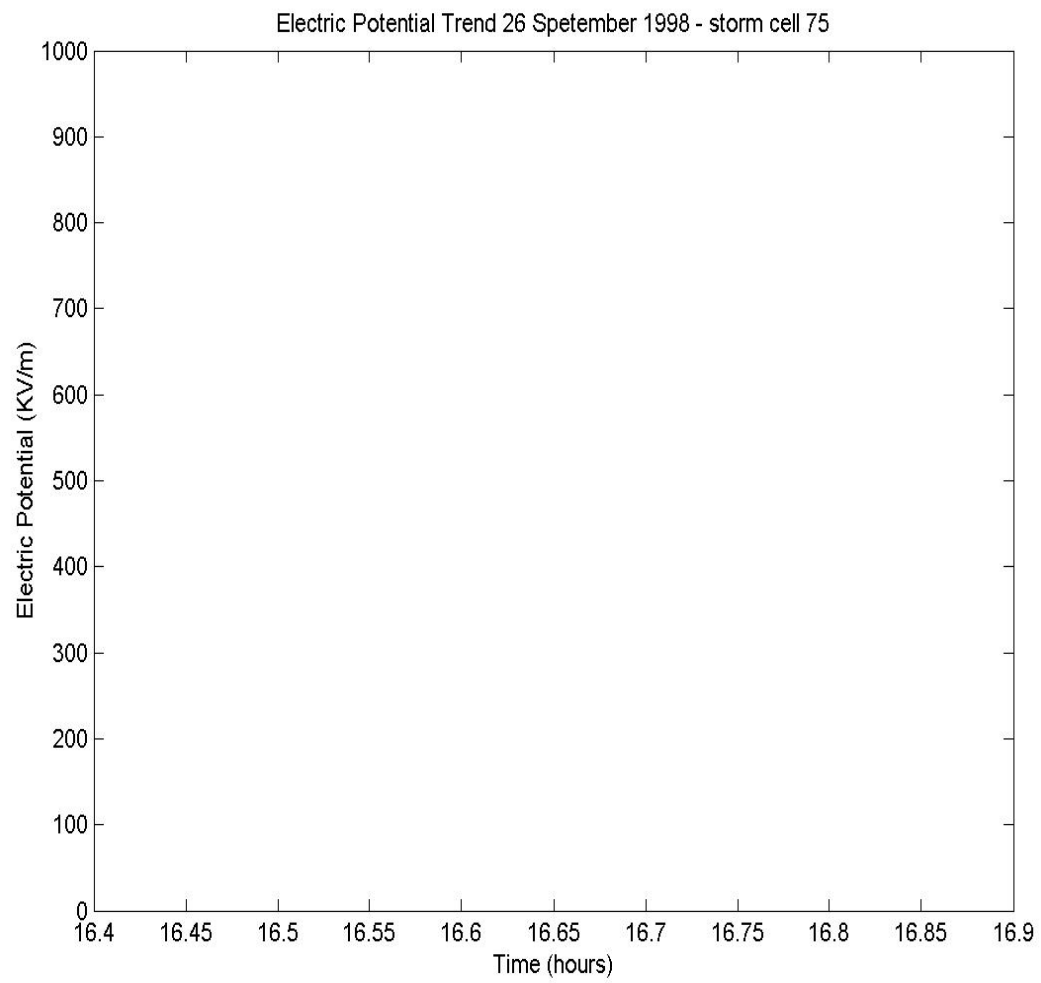


Figure A.9: Time vs. Electric Potential trend for storm #2

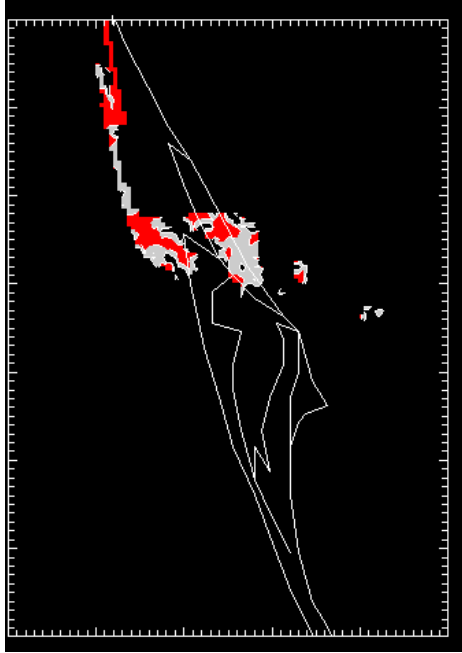


Figure A.10 (a): 0° C level at 16:25:58

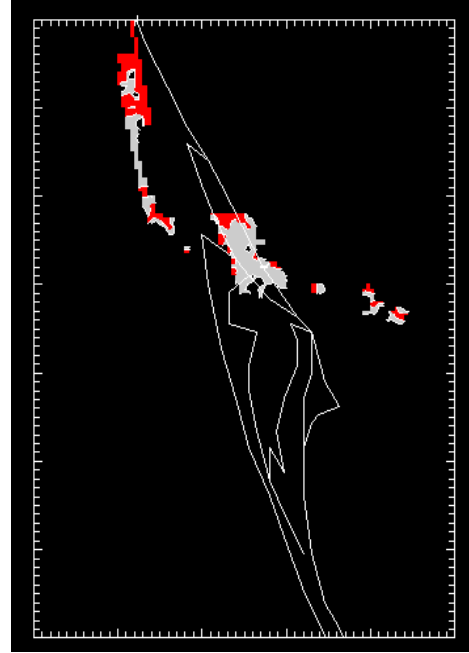


Figure A.10 (b): 0° C level at 16:31:10

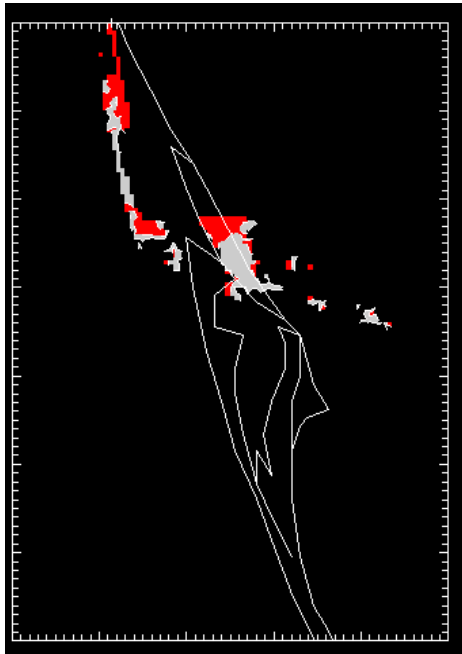


Figure A.10 (c): 0° C level at 16:36:22



Figure A.10 (d): 0° C level at 16:41:35



Figure A.10 (e): 0° C level at 16:46:47

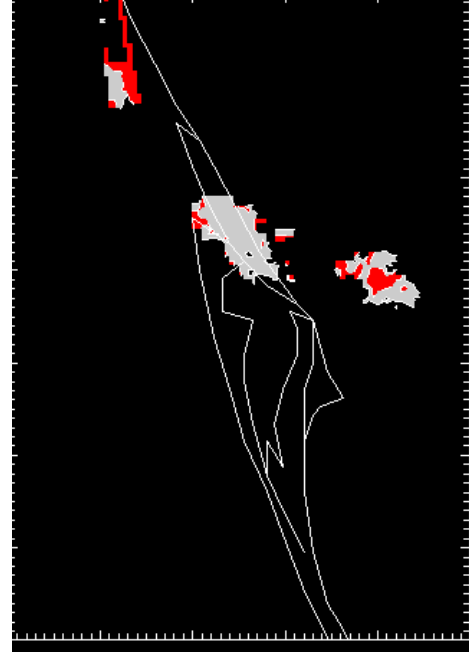


Figure A.10 (f): 0° C level at 16:51:49

Figure A.10: Ice- graupel- hail trends at the 0° C level for storm #2

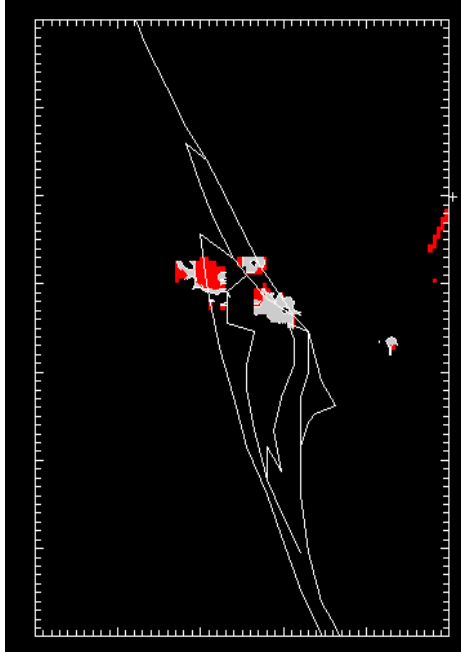


Figure A.11 (a): -5° C level at 16:26:04

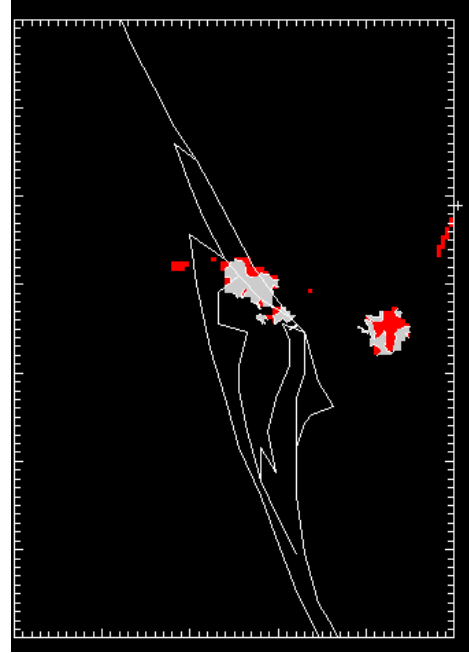


Figure A.11 (b): -5° C level at 16:31:16

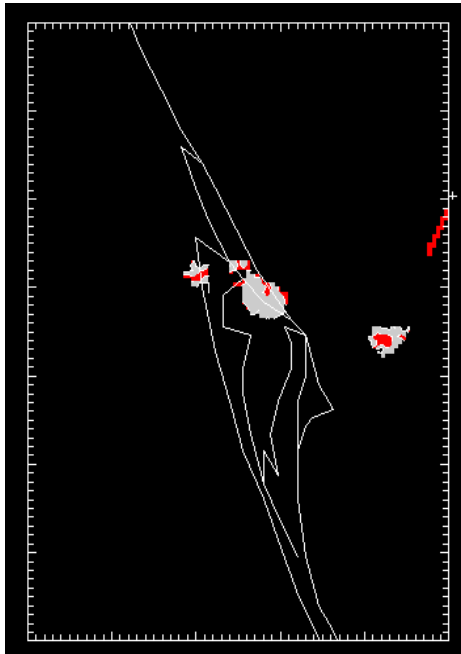


Figure A.11 (c): -5° C level at 16:36:29

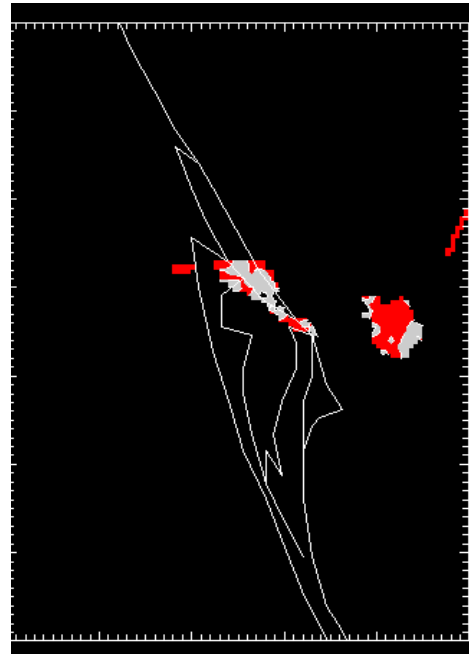


Figure A.11 (d): -5° C level at 16:41:41

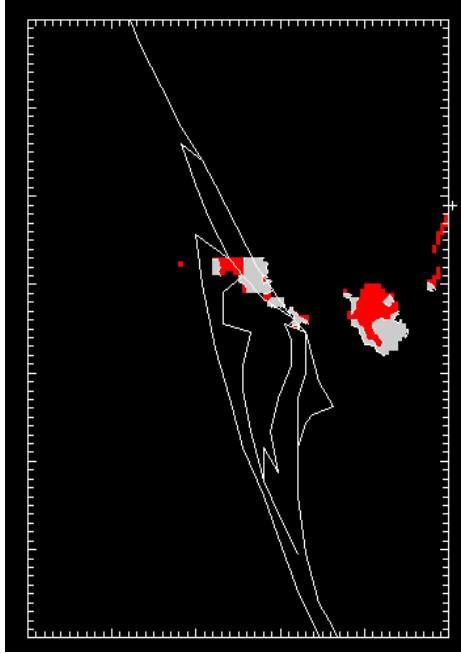


Figure A.11 (e): -5° C level at 16:46:53

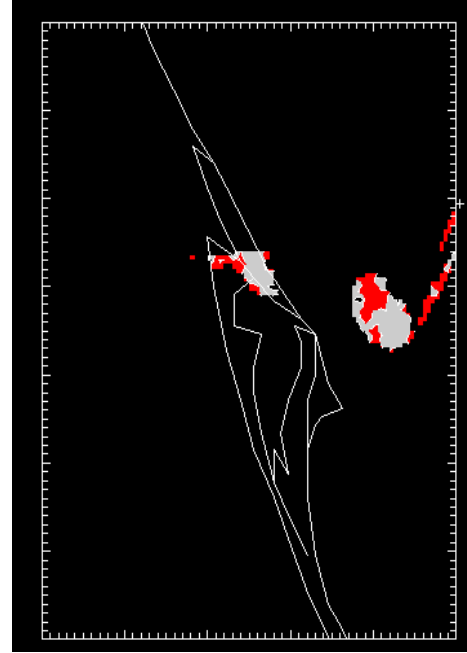


Figure A.11 (f): -5° C level at 16:52:06

Figure A.11: Ice-graupel-hail trends at the -5° C level for storm #2

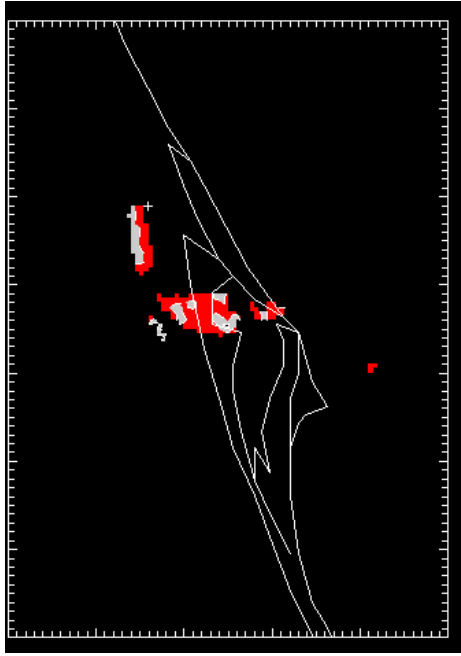


Figure A.12 (a): -10° C level at 16:26:10

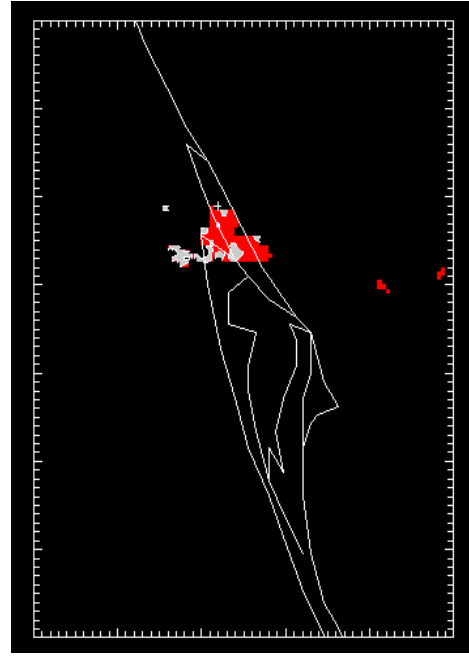


Figure A.12 (b): -10° C level at 16:31:23

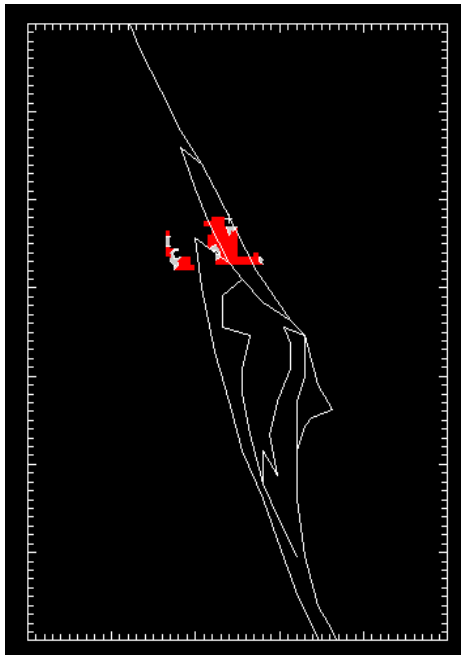


Figure A.12 (c): -10° C level at 16:36:35

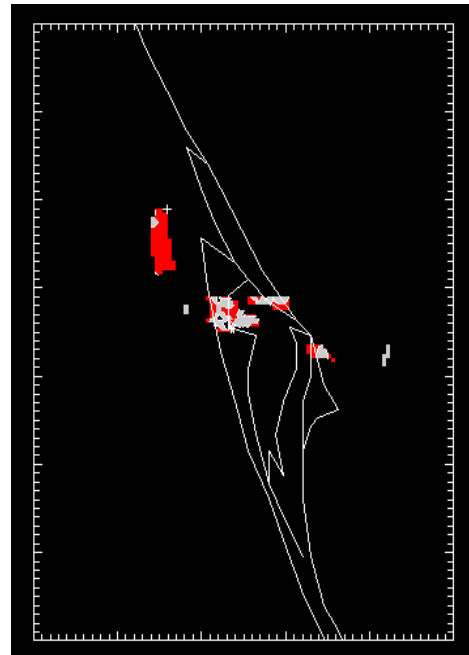


Figure A.12 (d): -10° C level at 16:41:41

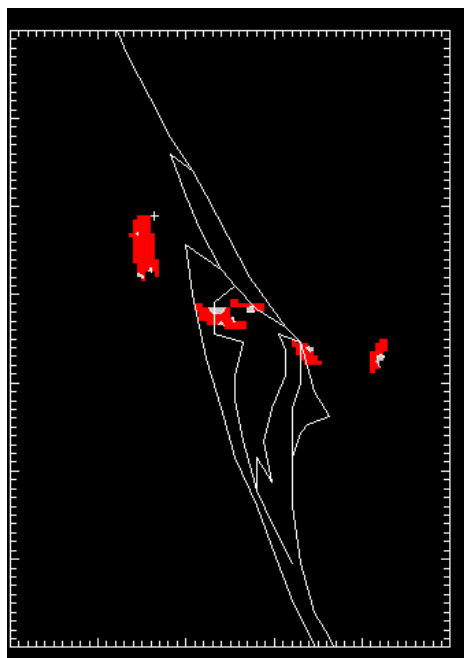


Figure A.12 (e): -10° C level at 16:46:53

Figure A.12: Ice-graupel-hail trends at the -10° C level for storm #2

LIST OF REFERENCES

1. Bedrick, M., and W. Burgett, 1999: A tropical oceanic cloud-to-ground lightning study. Preprints, 23rd Conference on Hurricanes and Tropical Meteorology, January 10-15, Dallas, Texas, American Meteorological Society, Boston, 243-245.
2. Bringi V.N., 2001: Polarimetric Doppler weather radar principles and applications
3. Doswell Charles, R. Davies-Jones, and D. Keller, 1990: *On summary measures of skill in rare event forecasting based on contingency tables. Wea. Forecasting*, 5, 576-585.
4. Gremillion, M. and R. E. Orville, 1999: *Thunderstorm characteristics of cloud-to- ground lightning at the Kennedy Space Center, Florida: A study of lightning initiation signatures as indicated by the WSR-88D radar, Wea. Forecasting*, 14, 640-649.
5. Hodanish, S.D. Sharp, W.Collins, C.Paxton, and R.E. Orville, 1997: *A 10-year monthly lightning climatology of Florida: 1986-95. Wea. Forecasting*, 12, 439-448.
6. S.G. Hoffert, and M.L. Pearce, 1996: *Lightning forecasting studies at Kennedy Space Center using WSR-88D and companion data sets. Preprints*, 15th Conference on Weather Analysis and Forecasting, August 19-23, Norfolk, Virginia, American Meteorological Society, Boston, 447-450.
7. Hondl, K.D., and Eilts, M.D, 1994: Doppler radar signatures of developing thunderstorms and their potential to indicate the onset of cloud-to-ground lightning, *Mon. Wea. Rev.*, 122, 1818-1836.
8. Jameson, A. R., M. J. Murphy, and E. P. Krider, Multiple-parameter radar observations of isolated Florida thunderstorms during the onset of electrification, *J. Appl. Meteorol.*, 35 (3), 343-354, 1996.

9. Lopez E.R, and Jean-Pierre Aubagnac: The lightning activity of a hailstorm as a function of changes in its microphysical characteristics as inferred from polarimetric radar observations
10. Lutz, J., B. Rilling, J. Wilson, T. Weckwerth and J. Vivekanandan, 1997: *S-Pol after three operational deployments, technical performance, siting experiences, and some data examples*. Preprints, 28th Conf. on Radar Meteorology, Austin, TX, 7-12 September. Amer. Meteor. Soc., Boston, 286-287.
11. Zipser, E.J., and K. Lutz, 1994: The vertical profile of radar reflectivity of convective cells: A strong indicator of storm intensity and lightning probability? *Mon. Wea. Rev.*, 122, 1751-1759.
12. Maekawa Y., Fukao S., Sonoi W., and Masukura K.: *Height distribution of ice particles in wintertime thunderclouds observed by a dual-polarisation radar*, Geoscience and Remote Sensing Symposium, 1994. IGARSS '94. 'Surface and Atmospheric Remote Sensing: Technologies, Data Analysis and Interpretation', International
13. Michimoto, K., 1991: *A study of radar echoes and their relation to lightning discharge of thunderclouds in the Hokuriku district. Part I: Observations and analysis of thunderclouds in summer and winter*. *J. Meteor. Soc. Jpn.*, 69, 327-66.
14. Roeder, W.P. and D.E.Harms, 2000: *Using climatology to improve weather forecasting for America's space program*. 12th Conf. on Applied Climo., Asheville,NC,7-11, May 00. 4 pp
15. Roeder, W.P., and C. Pinder, 1998: *Empirical techniques for central Florida lightning forecasts in support of America's space program*, Preprints, 16th Conference on Weather Analysis and Forecasting, Amer. Meteor. Soc., 475-477.

16. Ryzhkov A.V and Zrnic D.S: Observation of a MCS with a dual-polarisation radar
 Schaefer, T.J. The Critical Success Index as an indicator of warning skill, *Wea. Forecasting*,
 5,570-575
17. Scott R., Chen, T. and Krehbiel P.: Remote sensing of tropospheric clouds with a dual
 polarization radar
18. Soars, Maribel, 2001: Analysis of thunderstorm data from the STEPS project
19. Vivekanandan J., D.S. Zrnic, S.M. Ellis, R. Oye, A.V. Ryzhkov, J. Straka, 1999: *Cloud
 microphysics retrieval using S-band dual-polarization radar measurements*, *Bull. Amer.
 Meteorol. Soc.*, 80, 381-388.
20. Qie, Y. Yu, X. Liu, C. Guo, D. Wang, T. Watanabe, T. Ushio: Charge analysis on lightning
 discharges to the ground in Chinese inland plateau (close to Tibet), *Annales Geophysicae*,
 ISSN: 0992-7689 (printed version), ISSN: 1432-0576 (electronic version), Abstract Volume
 18 Issue 10 (2000) pp 1340-1348.
21. Handbook of atmospheric electrodynamics- volume 1
22. Penn State Thesis: Forecasting of cloud-ground lightning by the analysis of layered vertically
 integrated liquid
23. WDSS – II user documentation: <http://www.cimms.ou.edu/~lakshman/WDSS2/>
24. REORDER user documentation: <http://www.atd.ucar.edu/rdp/home/reorder.html>
25. CEDRIC user documentation : http://box.mmm.ucar.edu/pdas/Postscript/cedric_doc.ps
26. SOLO user documentation: http://www.atd.ucar.edu/rdp/solo/solo_home.html
27. <http://thunder.msfc.nasa.gov>